GOVERNMENT COLLEGE OF ENGINEERING AND CERAMIC TECHNOLOGY

Established 1941

Accredited by NAAC with Grade A

(2015)

Sample Evaluated project report/field work report submitted by the students

73, Abinash Chandra Banerjee Lane

Kolkata-700010

West Bengal, India

E-mail: gcectwb@gmail.com

Project work is compulsory for all five programmes. Two sample project works are submitted here.

First one, which is published as a journal paper in a reputed international journal, was done as a project work for the partial fulfillment of the M.Tech program in Information Technology. The URL of the paper is

Chakraborty, S., Chatterjee, K. & Dey, P. Discovering Tampered Image in Social Media Using ELA and Deep Learning. *SN COMPUT. SCI.* 3, 392 (2022). https://doi.org/10.1007/s42979-022-01311-w

Second project, which was done as the partial fulfillment of B. Tech degree in Ceramic Technology   was presented as a paper in 82nd Annual session of Indian Ceramic Society

DETECTION OF PASSIVE IMAGE TAMPERING
USING DEEP LEARNING

A PROJECT REPORT

Submitted by

SUNEN CHAKRABORTY

in partial fulfilment for the award of the degree

of

M.TECH

IN

INFORMATION TECHNOLOGY

2018-2020

GOVT. COLLEGE OF ENGINEERING AND CERAMIC TECHNOLOGY

**73, Avinash Chandra Banerjee Lane,
Beliaghata, Kolkata-700010**

BONAFIDE CERTIFICATE

Certified that this project report "......................DETECTION OF PASSIVE IMAGE TAMPERING USING DEEP LEARNING..................................."
is the bonafide work of "............SUNEN CHAKRABORTY..................."
who carried out the project work under my supervision.

SIGNATURE 14.7.21.

Dr.Mousumi Maitra
HEAD OF THE DEPARTMENT

Department: Information
Technology

P. Dey 14/07/21
SIGNATURE

Mrs. Paramita Dey
SUPERVISOR

Assistant Professor
Department: Information
Technology

Kingshuk Chatterjee 14.7.21
SIGNATURE

Dr. Kingshuk Chatterjee
SUPERVISOR

Assistant Professor
Department: Computer
Science &
Engg.

Full address of the Dept & College
Govt. College of Engineering & Ceramic Technology
73, Abinash Chandra Banerjee Lane
Kolkata-700 010

S.Roy 14.7.21
SIGNATURE

External Examiner: Dr. Sarbani Roy
Professor, Department of Computer Science & Engineering
Jadavpur University

ACKNOWLEDGEMENT

I would like to express my special thanks of gratitude to all of the Professors &

Asst. Professors in IT Department, specially thankful for being under the

supervision of **Mrs. Paramita Dey(Supervisor)** and **Dr. Kingshuk**

Chatterjee(Supervisor), for giving me the golden opportunity to do this project

on the "**DETECTION OF PASSIVE IMAGE TAMPERING USING DEEP**

LEARNING", which also help me in doing a lot of research. I came to know

about so many valuable and new things.

I am really thankful to them as they helped me a lot in finalizing this project

within the limited time frame.

Name: Sunen Chakraborty *Sunen Chakraborty*

Roll no.: GCECTM-R18-2009

Registration no. : 181130410011 of 2018-19

Semester: 4th

Year: 2018-2020

Department: Information Technology

ABSTRACT

In an era of digital images, the process of tampering an image became a common thing. Most of the time the tampering is done with such finesse that it can deceive human eyes. Availability of advanced software tools like Adobe Photoshop, GNU Image Manipulation Program (GIMP), and CorelDRAW can be used to create tampered pictures in a matter of minutes. Traditional methods that use handcrafted features and laid the foundation of tampering detection are not that efficient anymore. However, emergence of Deep Learning proves to be an effective method to detect changes in an image. These methods have greater accuracy than traditional methods because they can extract complex features from an image at a faster rate. They are also automatic which saves time and effort. Deep learning methods can achieve even more if they are used in company with some other techniques that can identify the underlying causes of the tampering. Here we experimented with Error Level Analysis and high-pass filters designed for Spatial Rich Model in steganalysis to increase the accuracy of the deep learning model.

TABLE OF CONTENTS

TABLE OF FIGURES

List of Abbreviations

1. ELA – Error Level Analysis

2. SRM – Spatial Rich Model

3. CNN – Convolutional Neural Networks

4. DNN - Deep Neural Network

5. RNN - Recurrent Neural Network

1. INTRODUCTION

1.1. Image Tampering

Image tampering is a kind of activity where one or multiple techniques are performed on digital images using any image editing software that alters the content of the images. Most of the time this is done for fun, but there are certain cases where image tampering is used for harmful schemes. The basic purpose is either to conceal an object in the scene or add a new object to the scene. Sometimes tampering of an image is done so meticulously that it is difficult to identify the altered regions. Nowadays an image can be tampered within minutes due to advancements in photo editing software like Adobe Photoshop, GNU Image Manipulation Program (GIMP), CorelDRAW, etc. Image tampering is also known as image forgery or image manipulation.

Figure.1 Example of Image Tampering

1.2. Image Tampering Detection

It would be very easy for an individual to locate the tampered regions by finding the difference between original and altered picture. However, when one is given a tampered image without its original as the reference, it is difficult to decide whether the picture is real or fake. According to the researchers image tampering detection can be classified into two categories (i) Active and (ii) Passive.
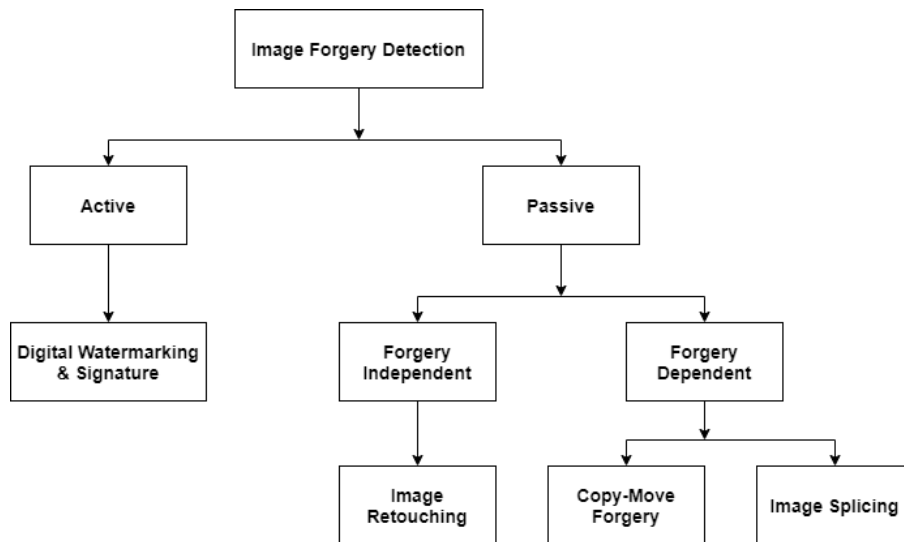
Figure.2 Types of Tampering Detection

1.2.1. Active Detection

In this kind of technique some code (like a signature or a watermark) is embedded into the image when it is created. Verifying this code authenticates the originality of image. Major drawbacks of this procedure are that the code needs to be inserted at the time of image creation and also it needs specialized hardware and software for this task.

1.2.2 Passive Detection

Passive / Blind detection techniques works in the absence of an embedded code. These are more difficult to detect than their active counterpart because the tampering can be done using an ordinary digital camera and any basic photo-editing software. Although in most cases one cannot distinguish between original and tampered images, this kind of techniques works on the principle that tampering might have changed the fundamental statistics of an image.

1.2.2.1 Forgery independent

This forgery type is based on artifact traces left during process of re-sampling, re-shaping & due to lighting inconsistencies. Image retouching belongs to this

category. It is considered quite harmless than the other type. Example of image retouching is shown in Figure 3.
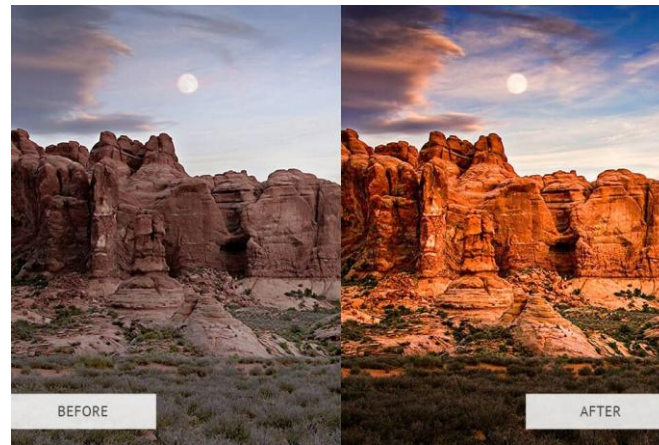
Figure.3 Image Retouching

1.2.2.2 Forgery dependent

These methods are designed to detect only certain type of forgeries such as copy-move and splicing. These are quite harmful and harder to detect.

1.2.2.2.1 Copy-Move Tampering and Detection

In copy-move tampering, part of an image is selected and it is pasted to another part of the same image. The basic purpose is either to conceal an object in the scene or add an additional object to the scene. This leads to a high similarity between these two regions which are shown in Figure 4.

(a) The original images   (b) The copy-move forged images
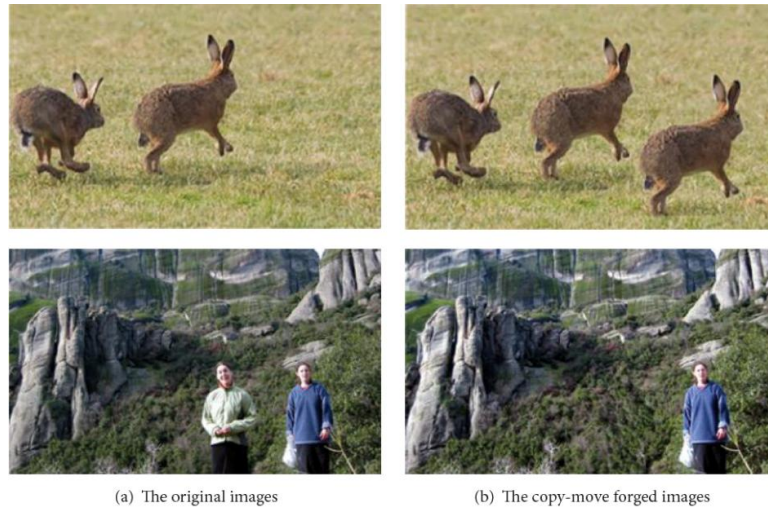
Figure.4 Copy-Move Tampering

The objective of this method is to detect duplicated regions in the given image. Correlation between multiple regions of an image indicates copy-move tampering. Traditional methods for the detection of Copy-move tampering can be classified into two kinds –

(i) Block based detection-

Here, an image is first broken into smaller square like regions called blocks and then features are extracted using certain algorithms. Multiple detection methods like DCT [1], PCA [2], DWT [3], and SVD [4] were proposed.

(ii) Keypoint Based Detection-

High entropy regions called keypoints of an image is identified. Then features are extracted using appropriate algorithms. Most popular algorithms for detecting keypoints are SIFT [5] [6] and SURF [7] [8].

After extracting features from an image using either of the techniques describe above, it is checked whether multiple areas contain same features to determine if that image has undergone tampering. Basic steps for copy-move forgery detection are shown in Figure 5.
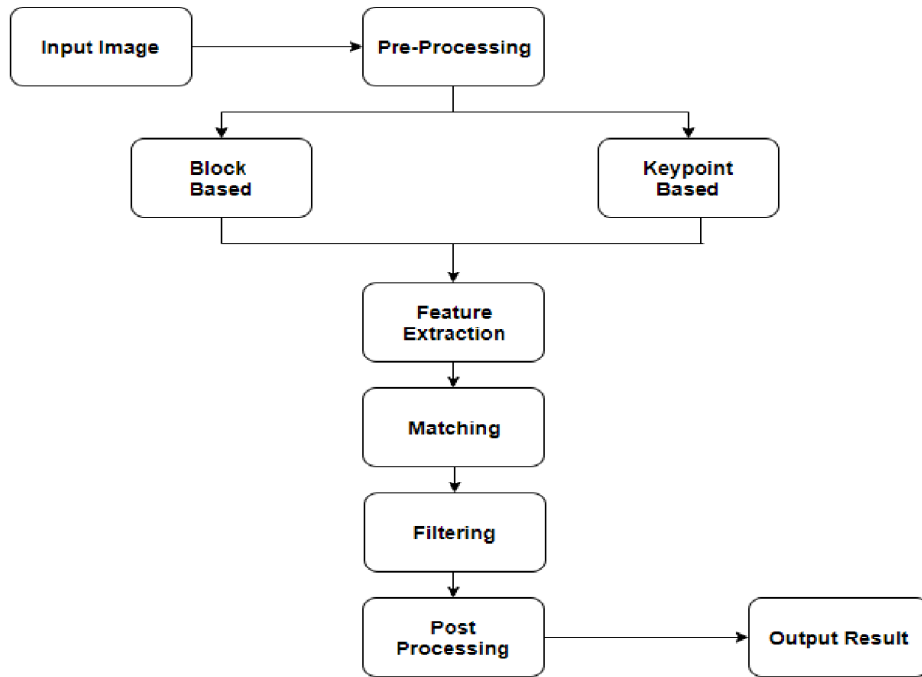
Figure.5 Basic steps for copy-move detection

1.2.2.2.2 Image Splicing and Detection

Image splicing is a very popular form of digital image tampering where certain contents from two or more images are combined together to create a finalized image. In case of image splicing regions with duplicated objects are absent unlike copy-move tampering. Due to this reason detection of image splicing is more difficult than detection of copy-move forgery. An instance of image splicing is illustrated in Figure 6.

(i) Authentic images   (ii) Spliced image

Figure.6 Image Splicing

Methods regarding detection image splicing focuses on the traces of tampering left on the image after it had undergone splicing. When an object is spliced from one image into another, sometimes it gives rise to sharp edges around that object and disrupts the edges that were originally there, this leads to edge discontinuity [9]. Another way is that different camera manufacturers configure their devices differently, if splicing is done using images from dissimilar camera models then there will be a difference in lighting effects [10] [11]. When someone uses JPEG images for tampering and resaves the forged image into JPEG format, then two compression operations occurs, this lead to situation called double quantization (DQ) effect [12].

1.3 Disadvantages of Traditional detection techniques

Traditional techniques are also called as hand-crafted techniques because each of these techniques is able to detect only certain kind of tampering. Images which are tampered in a different way need algorithms tailored to detect only that specific tampering [13]. Also these techniques can extract simple features only, which mean they don't perform well if the images have undergone extensive post-processing to hide the signs of tampering [13]. At last, most of these methods are tested only on a handful of images.

1.4 Advantages of Deep learning

Advancement in the GPU technologies and the success of Deep Learning techniques in the field of computer vision motivated the researchers to apply DL models for image forgery detection. Deep learning techniques are data-driven and capable of automatically learning complex features, necessary to identify tampered regions for the classification phases [14]. Moreover, it also saves time and energy required to find hand-crafted features from tampered images. There are Deep learning modes such as Convolutional Neural Networks (CNN), Deep

Neural Network (DNN), and Recurrent Neural Network (RNN). Convolutional Neural Networks (CNN) is popular amongst these models.

2. Literature Review

To detect tampering Rao et al. [15] initialized the first layer of CNN with high-pass filters that captures objects generated during the tampering. The CNN is used to draw out features from the images patch-wise, and then features are combined using a fusion method to obtain the final features for classification. Chen et al. [16] introduced a filter layer in his network, where this layer is used to discard unnecessary information and help to detect residuals of median filtering done on an image to hide the evidence of any tampering. Zhang et al. [14] divide images into patches, and then deep learning Stacked Autoencoder (SAE) is used for feature learning of individual patch, after that contextual information was incorporated into individual patch to detect tampered regions. Huang et al. [17] focus on how to detect various post-processing done to hide the traces of tampering. First, a proposed steganalysis means is used to get the features from the images. Then a CNN is used to scan the features using a sliding window approach, a fusion technique is used to obtain the final features. At last, classification of different operations is done. Zhou et al. [18] proposed a faster region-based CNN consisting of two branches. In its first branch colour images are fed directly for obtaining the features and classifying the tampering style. In the second branch suggested filters are used to detect noise alterations in case the forger performs post-processing. Finally, a method is employed to fuse the output of both the branches to localize altered regions as well as classify tampering style.

3. Methodology

In this section we will be describing the mechanism of our experiment in full details.

3.1 Error Level Analysis (ELA)

The idea of ELA was proposed by Neal Krawetz et al. [19]. This technique is performed on an image that uses lossy compression, mostly JPEG images. If an image of JPEG format is tampered and resaved as a JPEG image again, then some of its information is lost after compression. The task of ELA is to resave an image at a notable error rate of 95% compression, and evaluating the difference between the original image and resaved image. Since JPEG images consist of 8×8 blocks, after compression all of the blocks should have almost similar error levels. In the case of tampering, modified areas can be easily identified because 8×8 blocks of these areas will have a different error level than the areas that have not been modified. ELA of an authentic image is shown in Figure 7 while ELA of a tampered image is shown in Figure 8.
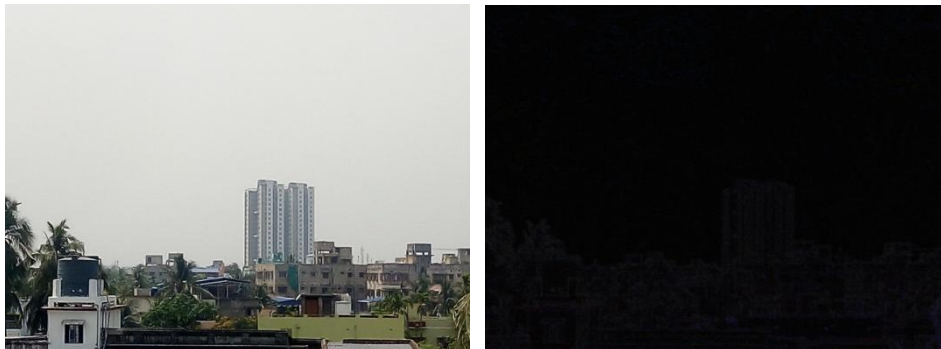
Figure.7 ELA of an authentic image

Figure.8 ELA of a tampered image

3.2 Spatial Rich Model (SRM)

SRM is a very powerful technique in the field of steganalysis that is used to detect significant features in an image. It basically computes the statistics needed to discover certain features from the noise residuals present in the neighbourhood in an image. As the residuals are linked with the image content, changes in the content will affect those residuals. Before the emergence of deep learning, SRM was considered as the most successful approach to discover changes in an image. Still many researchers came to the conclusion that using deep learning models with the noise residuals of SRM leads to even greater performances [15] [16] [17][18]. SRM utilises several high-pass filters [20] to get diverse noise residuals of image which are shown in Figure 9.
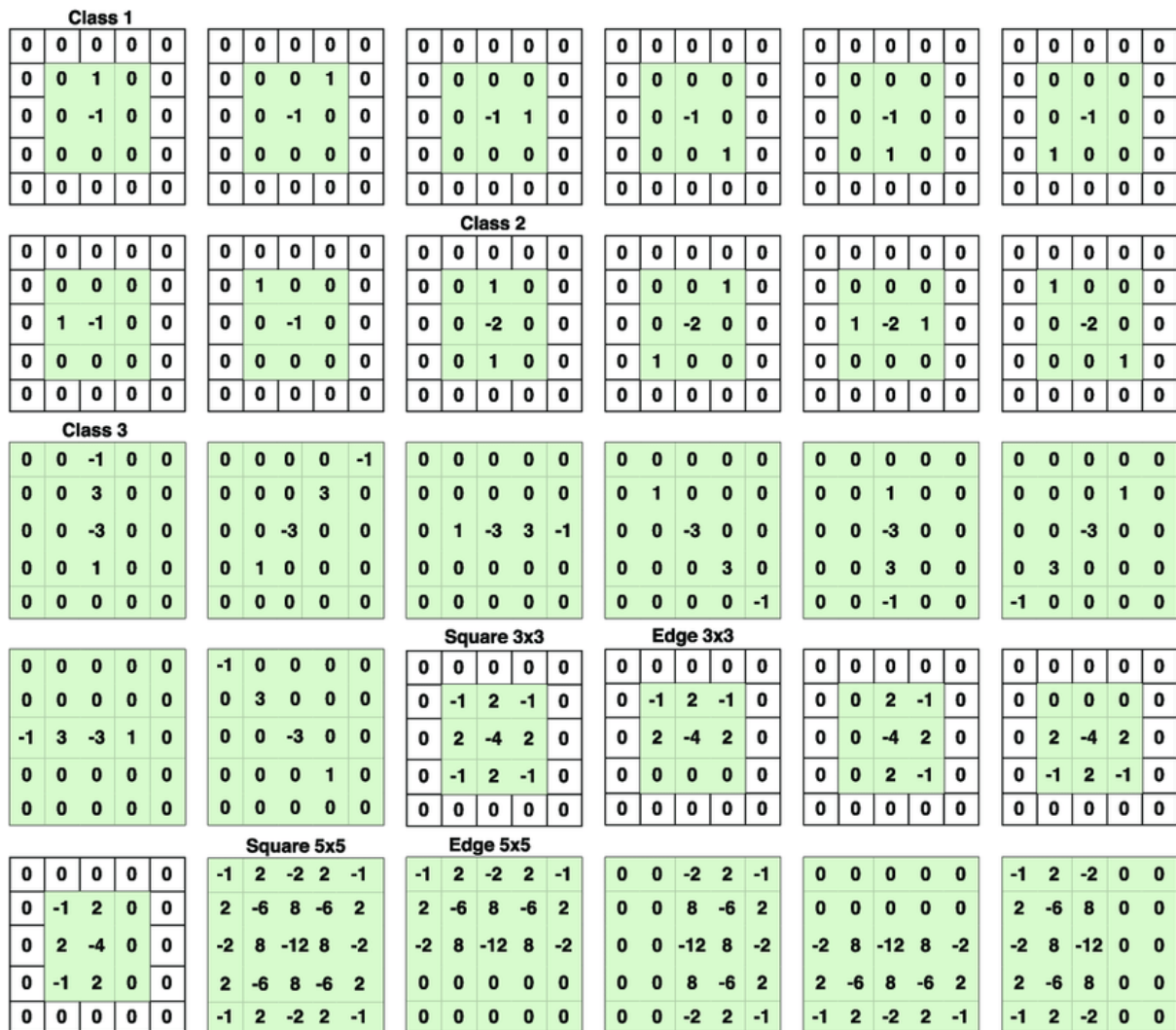
Figure.9 SRM filters for noise residuals

Noise residual image obtained after passing an image from these 30 filters is shown in Figure 10.
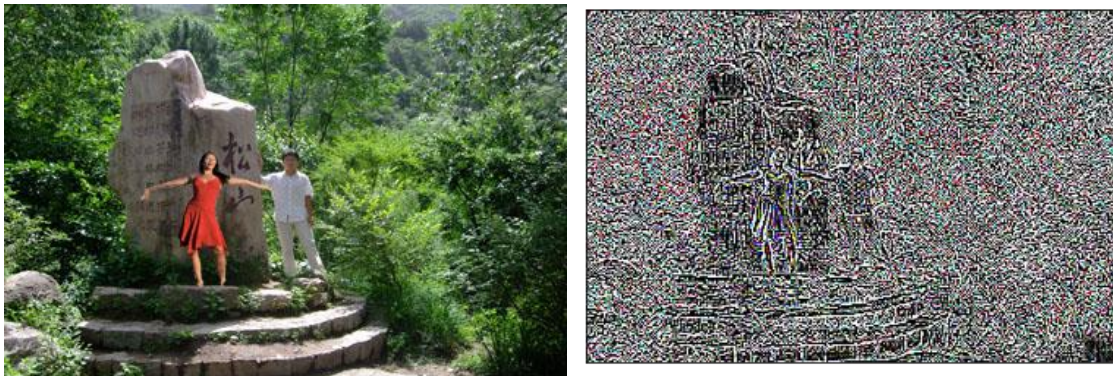
Figure.10 Noise Residuals of an image

3.3 Convolutional Neural Networks (CNN)

Convolutional Neural Networks was designed by LeCun et al. [21], where it was employed to recognize hand-written digits from the images. The function of the CNN is to minimize the data into a structure that is pretty straightforward to compute, without missing those features which are fundamental for getting a good outcome. CNNs are mostly utilized for working with 2-Dimensional data like images or videos. Just like any other neural network CNNs also have three kinds of layers, input layer, hidden layers, and output layer. Elementary architecture of a CNN is shown below in Figure 11.
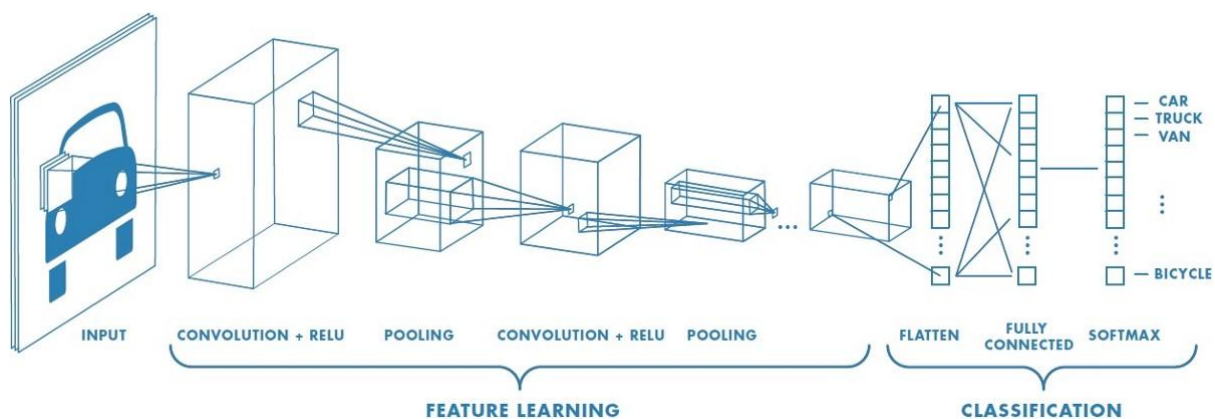
Figure.11 Basic architecture of CNN

3.3.1 Convolutional Layer

The primary operation that a CNN apply on the data is convolution which transforms the data into a map that depicts the key features, which is called feature map. This layer is the principle element of the neural network. First an input layer of shape: (input image height) x (input image width) x (input image channels) accepts the data, and forward it to a convolutional layer which is a set of filters/ masks/ kernels used to extract the features. A filter is a matrix of shape m x n. Every filter slide across the width and height of an image to perform convolution, which means to compute dot product of the filter with a part of an image whose size is similar to that of the filter. Individual filter is designed to extract a certain feature from an image. *Proposed model uses eight convolutional layers.*

3.3.2 Pooling Layer

When the convolutional layer creates the feature maps, those maps carry way too much spatial information. This increases the load on the computational resources which increases the time taken for training the network. Those maps also carry information not needed by the network, like the positions of the features rather than their relationships and priority. Pooling layers are uses a method which reduce the size of those maps and makes it simpler to deal with the information. This makes the model more robust and helps the model train faster. There are three kinds of pooling, max pooling, average pooling, and global pooling.

In max-pooling, only the maximum element will be extracted from the area covered by the filter. In this manner, only important elements from each feature of the feature map are considered.

In average-pooling, average of all the elements will be extracted from the covered by the filter. Hence, averages of all features are present in the output.

In global-pooling, all the elements of an entire feature map are converted into a single element. Global-pooling can be used either like max-pooling or average pooling.

Proposed model uses four max-pooling layers.

3.3.3 Concatenation Layer

A concatenation layer accepts the output of two or more different layers as inputs and concatenates them along a particular axis. The inputs must have the similar dimensions except the concatenation dimension. *Proposed model uses one concatenation layers.*

3.3.4 Fully Connected Layer

These are the last layers in a CNN. It performs classification operations like an artificial neural network dependent on the information extracted by the preceding layers of a CNN. Output from the last convolutional or pooling layer in a 3-Dimensional format must be converted into a 1-Dimensional vector before passing it into the fully-connected layer. *Our model uses one fully connected layer and a two-way softmax layer.*

3.3.5 Output Layer

The output layer is generally a layer with softmax activation function which converts the input vector of the fully connected layer into a probability vector that generates the probability of each class label in the CNN.

3.3.6 Tuning Parameters

During training period we need to change the parameters of the model to bring down the loss as much as possible which will help our model to make more accurate predictions thus optimizing it further. The algorithms or methods which help us to modify these parameters are called optimizers. To tune our

model during training, we used "*RMSprop*" [22] as the optimizer. After passing the result using the "softmax" function, the function utilized to minimize the variation between actual result and predicted result is called loss function. Here we have used "*categorical_crossentropy*" as the loss function to tune our model. The complete architecture of our CNN is shown in Figure 12.
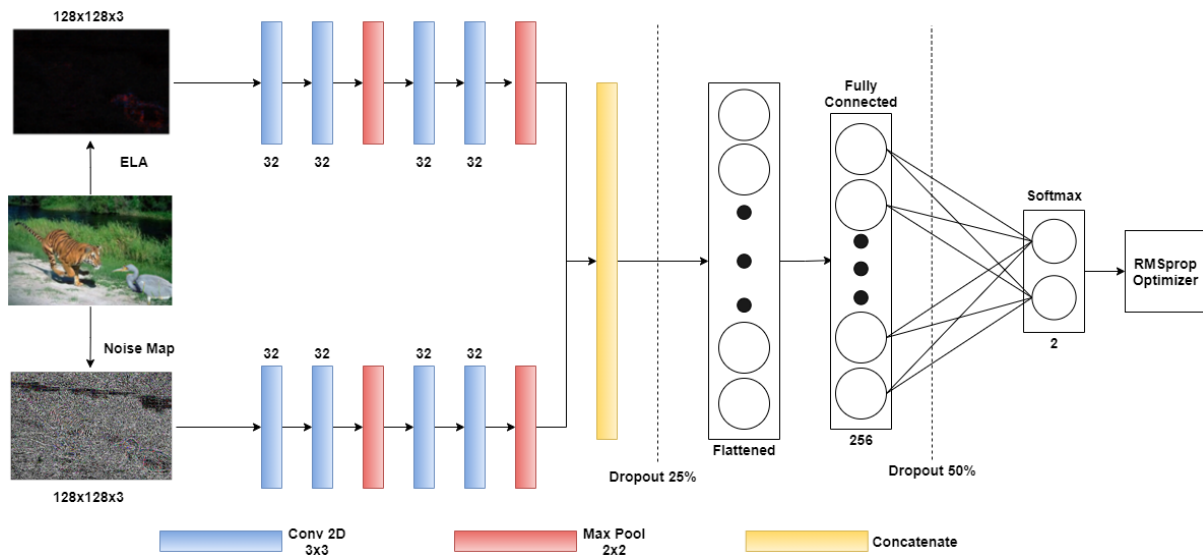
Figure.12 Proposed Dual Branch CNN

4. Resources Utilized

4.1. Setup

All of our experiments are conducted using Jupyter Notebook available on Google Colab. Training of the model is performed using a GPU runtime on Google Colab which assigned a RAM of 12.72 GB and a Disk Space of 68.40 GB. Colab has pre-installed packages needed for deep learning, but additional packages can be installed.

4.2. Dataset Used

For training our model we chose the CASIA dataset [23] available on Kaggle. More specifically we chose the CASIA v2.0 dataset because CASIA v1.0 dataset contains fewer samples. CASIA v2.0 dataset consists of 7492 authentic

images and 5124 tampered images of various lossy and lossless formats. We chose CASIA v 2.0 dataset because the images in CASIA v 2.0 are tampered in two ways. First one is copy-move tampering and second one is image splicing. Both copy-move and splicing are basic kinds of tampering, which is why this dataset is more suitable for tampering detection. Figure 13 shows samples of authentic images while Figure 14 shows samples of tampered images from the dataset.
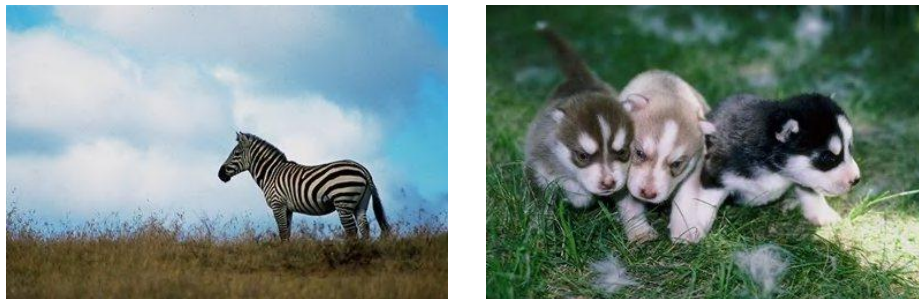
Figure.13 Authentic Samples from CASIA v2.0

Figure.14 Tampered Samples from CASIA v2.0

5. Experiment Results and Discussions

5.1 Training of the model

It was first observed by Chen et al. [16] that using tampered images directly as inputs to the CNN it is not suitable for tampering detection. As it learned the features of the images rather than the aspects related to tampering. Because of this many researchers focused on data pre-processing [17] while others created

tailored layers in their models that will do the pre-processing automatically [15] [24].

For our experiment we used two image pre-processing techniques which were mentioned previously to detect tampering. First we generated ELA of the images and then we find the noise residuals utilizing high-pass filters designed for Spatial Rich Model. Since ELA works well on images with lossy compression, we chose images with lossy format which is JPEG and discarded images of other formats. After that our dataset contained 5064 authentic and tampered images. After generating ELA and noise residuals of those images and adding their labels there is 5064 ELA images samples and 5064 noise residual samples. Then the data is split into 90% for training and 10% for validation. Then the images are fed into the dual-branch neural network for training up to 40 epochs. Complete workflow of our experiment is illustrated in Figure 15.
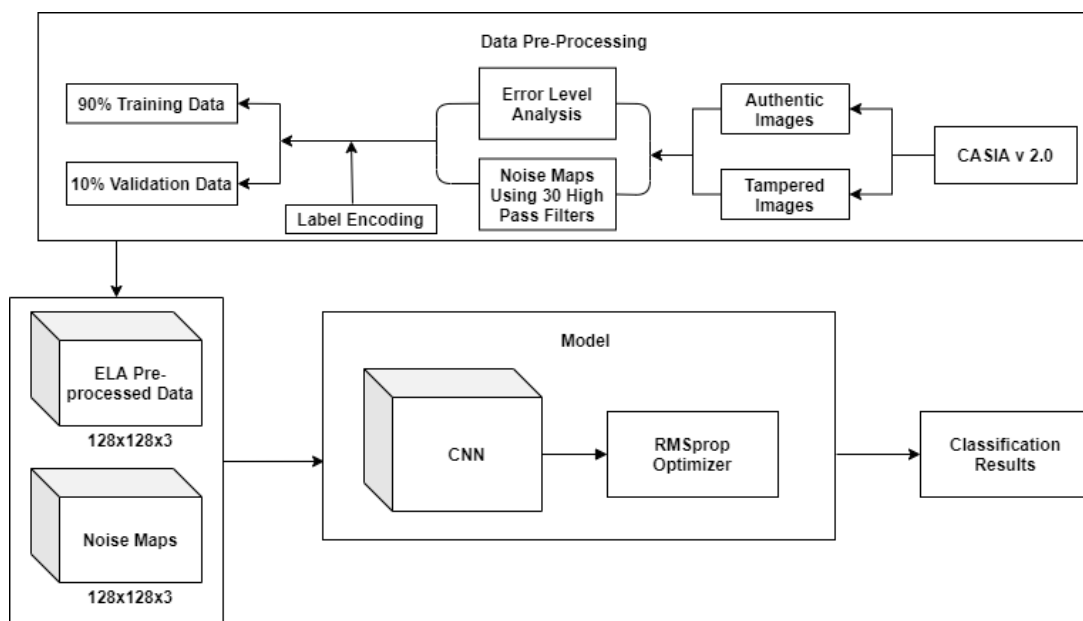
Figure.15 Complete workflow of the experiment

5.2 Performance of the model

The training process stops at epoch 17. The accuracy of the model is illustrated in Figure 16 while the loss is shown in Figure 17.
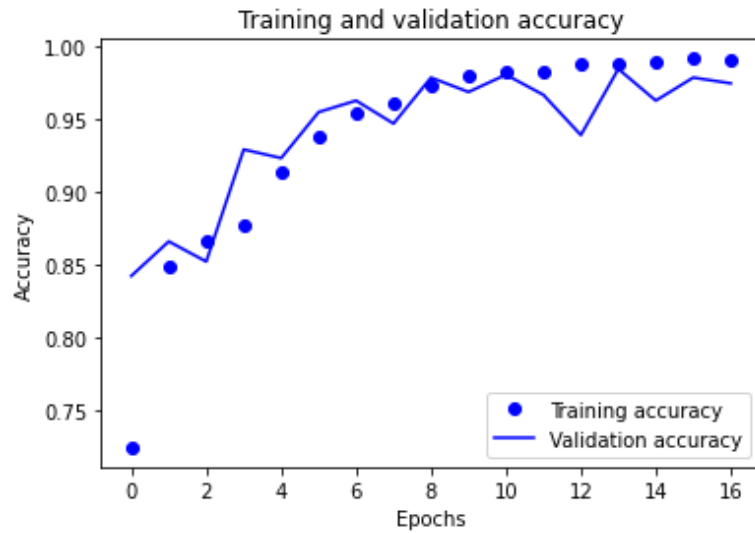
Figure.16 Accuracy Curve of the model
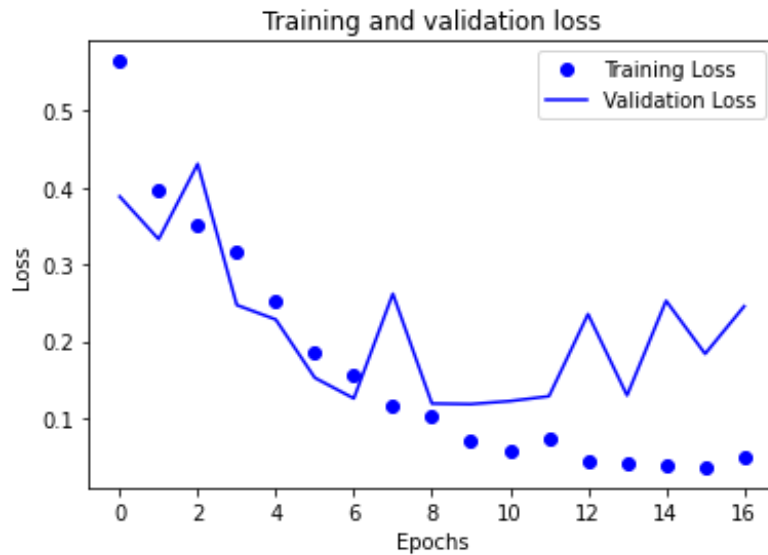
Figure.17 Loss curve of the model

As you can see from the figures above that our model achieved training accuracy of 98.99% and validation accuracy of 98.42%. Then we evaluate our model over the validation data whose confusion matrix is presented below in Figure 18.
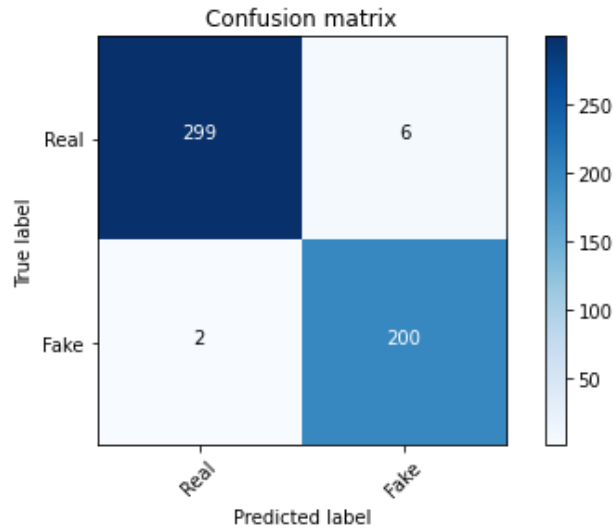
Confusion matrix

Figure.18 Confusion Matrix

From the confusion matrix shown above we can calculate precision, recall and f1-score of our model, whose formulae are shown below.

$$Precision = \frac{True\ positive}{True\ Positive + False\ Positive}$$

$$Recall = \frac{True\ Positive}{True\ Positive + False\ Negative}$$

$$F1\ Score = 2 \times \frac{Precision \times Recall}{Precision + Recall}$$

Also the calculated results of our model are illustrated in Table 1.

Precision	Recall	F1 Score
0.9934	0.9803	0.9868

Table.1 Precision, Recall and F1 Score of our model

6. Conclusion

The amount of tampered images we find these days makes us question the information we come across. Digital image forensics is having a tough time dealing with these kinds of fake information. Convolutional Neural Networks

have a remarkable performance when it comes to extracting features from images. But CNNs are inclined to learn features from the images rather than finding the signs of tampering.

Hence, to improve the effectiveness we pre-processed the images using Error Level Analysis and noise residuals from SRM, and then fed them to a CNN. The model can fairly classify between authentic and tampered images as it obtained an accuracy of 98.42%.

7. Reference

1. Fridrich AJ, Soukal BD, Lukáš AJ. "Detection of copy-move forgery in digital images". In in Proceedings of Digital Forensic Research Workshop 2003.

2. Popescu, A.C. and Farid, H. "Exposing digital forgeries by detecting duplicated image regions". 2004.

3. A. N. Myna, M. G. Venkateshmurthy and C. G. Patil, "Detection of Region Duplication Forgery in Digital Images Using Wavelets and Log-Polar Mapping," International Conference on Computational Intelligence and Multimedia Applications (ICCIMA 2007), 2007, Vol. 3, pp. 371-377

4. G. Li, Q. Wu, D. Tu, and S. Sun, "A sorted neighborhood approach for detecting duplicated regions in image forgeries based on DWT and SVD," in IEEE Int. Conf. Multimedia and Expo, Beijing, China, 2007, pp. 1750–1753.

5. Lowe DG. "Distinctive image features from scale-invariant keypoints". International journal of computer vision. 2004 Nov; 60(2): pp. 91-110.

6. Huang H, Guo W, Zhang Y. "Detection of copy-move forgery in digital images using SIFT algorithm". In2008 IEEE Pacific-Asia Workshop on Computational Intelligence and Industrial Application 2008 Dec 19, Vol. 2, pp. 272-276.

7. Bay H, Ess A, Tuytelaars T, Van Gool L. "Speeded-up robust features (SURF)". Computer vision and image understanding. 2008 Jun 1; 110(3): pp. 346-59.

8. Bo X, Junwen W, Guangjie L, Yuewei D. "Image copy-move forgery detection based on SURF". In2010 International Conference on Multimedia Information Networking and Security 2010 Nov 4. pp. 889-892.

9. Fang Z, Wang S, Zhang X. "Image splicing detection using color edge inconsistency". In2010 International Conference on Multimedia Information Networking and Security 2010 Nov 4. pp. 923-926.

10. Ng TT, Chang SF. "A model for image splicing". In2004 International Conference on Image Processing, 2004. ICIP'04. 2004 Oct 24. Vol. 2, pp. 1169-1172.

11. Johnson MK, Farid H. "Exposing digital forgeries by detecting inconsistencies in lighting". InProceedings of the 7th workshop on Multimedia and security 2005 Aug 1, pp. 1-10.

12. Popescu A.C., Farid H. (2004) "Statistical Tools for Digital Forensics". In: Fridrich J. (eds) Information Hiding. IH 2004. Lecture Notes in Computer Science, vol 3200. Springer, Berlin, Heidelberg. Pp. 128-147.

13. X. Bi, Y. Wei, B. Xiao and W. Li, "RRU-Net: The Ringed Residual U-Net for Image Splicing Forgery Detection," 2019 IEEE/CVF Conference on Computer Vision and Pattern Recognition Workshops (CVPRW), 2019, pp. 30-39

14. Y. Zhang, J. Goh, L. L. Win, and V. L. Thing, "Image region forgery detection: A deep learning approach." in *SG*-CRC, pp. 1–11, 2016.

15. Rao Y, Ni J. "A deep learning approach to detection of splicing and copy-move forgeries in images". In2016 IEEE International Workshop on Information Forensics and Security (WIFS) 2016 Dec 4, pp. 1-6.

16. Chen J, Kang X, Liu Y, Wang ZJ. "Median filtering forensics based on convolutional neural networks". IEEE Signal Processing Letters. 2015 Jun 1;22(11):pp. 1849-1853.

17. Huang T, Yuan X. "Detection and classification of various image operations using deep learning technology". In2018 International Conference on Machine Learning and Cybernetics (ICMLC) 2018 Jul 15, Vol. 1, pp. 50-55.

18. Zhou P, Han X, Morariu VI, Davis LS. "Learning rich features for image manipulation detection". InProceedings of the IEEE Conference on Computer Vision and Pattern Recognition 2018. pp. 1053-1061.

19. Krawetz N, Solutions HF. "A picture's worth". Hacker Factor Solutions. 2007;6(2):p 2.

20. Fridrich J, Kodovsky J. "Rich models for steganalysis of digital images". IEEE Transactions on Information Forensics and Security. 2012 May 8;7(3): pp. 868-882.

21. LeCun Y, Boser B, Denker JS, Henderson D, Howard RE, Hubbard W, Jackel LD. "Backpropagation applied to handwritten zip code recognition". Neural computation. 1989 Dec;1(4):pp. 541-551.

22. Tieleman T, Hinton G. "Lecture 6.5-rmsprop: Divide the gradient by a running average of its recent magnitude". COURSERA: Neural networks for machine learning. 2012 Oct;4(2):pp. 26-31.

23. Sovathana P, Kaggle. casia dataset. 2018.
https://www.kaggle.com/sophatvathana/casia-dataset.

24. Bayar B, Stamm MC. "A deep learning approach to universal image manipulation detection using a new convolutional layer". InProceedings of the 4th ACM workshop on information hiding and multimedia security 2016 Jun 20. pp. 5-10.

Effect of Bauxite & Zirconia Addition on the Densification and Microstructural Properties of Mullite Aggregates Derived from Sillimanite Beach Sand

A project submitted in partial fulfilment of the requirements for the degree

of

Bachelor of Technology
In
Ceramic Technology

Submitted by

Abhishek Das (GCECTB-R15-1001)

Tilak Matabbar (GCECTB-R15-1035)

Under the guidance of

Dr. Kaberi Das
Assistant Professor (Dept. of Ceramic Technology)

Government College of Engineering & Ceramic Technology

(An Autonomus Institution under MAKAUT, NAAC accredited A Grade)

Acknowledgement

With deep regards and profound respect, we avail this opportunity to express our deep sense of gratitude and indebtedness to **Dr. Kaberi Das (**Assistant Professor, Dept of Ceramic Technology, GCECT, Kolkata**)** for his inspiring guidance, constructive criticism and valuable suggestion throughout in this project work.

It was very enriching and enlightening experience to work under her guidance. she has been very helpful and supportive; without her support this project would not have been possible. It was she who took initiative to send us to give oral presentation in 82nd annual session of Indian Ceramic Society at Jamshedpur on 8-9th January, 2019. For all of these invaluable helps we will be ever grateful to her.

We thank our Principle **Prof.(Dr.) K. Chakraborty** for his encouragement. We also would like to express our gratitude to our professors **Dr. R. Sen, Dr. R.C. Das, Dr. T.K. Bhattacharya, Dr. S. Patra, Dr. B.K. Sanfui,** who give us support, guidance & suggestions throughout the project.

We thank Mr. Jiban Dey for assisting us every day in laboratory.

We are heartily thanks to **Ramkaran Mosalpuri** (PhD. Scholar, CU) & **Pameli Paul** (PhD. Scholar, CU)

We are grateful to University college of Science & Technology, Calcutta University, Razabazar, Kolkata, Indian Institute of Engineering Science and Technology, Shibpur and Central Glass & Ceramic Research Institute (CGCRI), Kolkata for carrying out our SEM, EDX and XRD.
 Lastly, we thank everyone who has helped us in all respect for giving our project a success.

Mr. Abhishek Das
(GCECTB-R15-1001)
Mr. Tilak Matabbar
(GCECTB-R15-1035)

B.Tech (Ceramic Technology)
GCECT, Kolkata.

Table of Contents

CHAPTER 1

INTRODUCTION

1. Introduction

Sillimanite, Andalusite and Kyanite complies the anhydride aluminium silicate polymorphs, commonly known as the Sillimanite group of minerals. Such minerals have the same composition ($Al_2O_3.SiO_2$) and transform into mullite and silica at temperature between 1300-1600°C depending on the polymorphic form, particle size and level of impurity. These raw materials are consumed primarily in refractory industry due to their transformation to mullite at high temperature. The mullite phase shows high hot strength with good resistance to chemical corrosion & physical erosion. [1]

Sillimanite group of minerals decompose to mullite and silica during thermal decomposition. These minerals show various characteristics of thermal expansion in which kyanite has the highest value. The nature of the silica that is liberatedon heating also varies. It is in the form of cristobalite for kyanite and amorphous silica for sillimanite and andalusite. SiO_2 released during thermal transformation and partially reacts with impurity to form a glassy phase, which impairs the product quality. Product quality can be improved by alumina to form more mullite.

$$3(Al_2O_3.SiO_2) = 3Al_2O_3.2SiO_2 + SiO_2$$

Mullite is widely used in various applications due to its several important properties such as good chemically inert, low thermal conductivity, high creep resistance, high refractoriness, low thermal expansion coefficient & good thermal shock resistance.

It is extremely rare natural material. Commercially mullite products are usually synthesized from various alumina and silica precursors through technique such as Co-Precipitation, Sol-gel, hydrothermal and chemical vapour deposition. In this process's alumina precursors are naturally γ-alumina, aluminium fluoride, aluminium hydroxide, α-alumina or other aluminium salts, whereas silica sources can be pure natural quartz, cristobalite, amorphous silica, colloidal, fumed and precipitated silica etc. However, mullite products produced from high purity reagents and precursors are not commercially available for bulk refractory applications. Normally, cheap, readily, locally, abundantly available natural raw materials are preferred to produce refractory-grade mullite aggregates. So far, raw materials used for this purpose include kaolinite, sillimanite and bauxite. Most of mullite obtained from these natural materials show an

inferior property in proportion to impurity levels.Further, a gradual depletion of the currently used raw materials represent a serious challenge to the refractory community to keep up the continuous production to mullite that as in high demand. Therefore, finding alternate alumina sources to meet the mullite requirement in term of production demand and properties has become imperative. Recently, beach sand sillimanite (BSS) has been identified as an alternative low-cost raw material which is abundantly available in nature. An estimated amount of BSS available in India about is 54 million tons, out of which a very small percentage is used in refractory industries and the rest remains unused as waste. The utilization of this mineral will contribute to environmental safety and to preserve valuable naturally occurring mineral resources. [2]

Sillimanite occurs in nature in rock form. But the rock form sillimanite has been depleted/exhausted in many parts of the world. Placer deposits of beach sand sillimanite minerals occur in a number of coastal areas. Placer deposits are two types, viz beach placers and inland placers. India is gifted with a coastline of over 6000km, hosts some of the largest and richest shoreline placers. Sillimanite beach placer deposits found in the eastern & southern coasts [3]

Previous studies revealed that the submicron sized BSS & alumina mixtures reacted to form mullite with 99% of the theoretical density after sintering at 1500-1575℃in presence of sintering aids. However, the use of submicron sized powders not viable for commercial production. Further precursors mixtures containing BSS with an average particle size (APS) of 5-6 µm require sintering temperature greater than 1700℃ to form dense mullite aggregates. Lowering the sintering temperature while achieving the same degree of densification and mullite phase transformation would have some distinct advantages, including energy savings, finer microstructure and hence improved mechanical properties. Volume expansion associated with the 3:2 mullite formation from aluminosilicates was found to be one of the main factors restricting the densification of the aggregates.

In the present work, in first phase of work bauxite was added with different amount as source of alumina with sillimanite beach sand. The bauxite amount was optimised. In the second phase of the study, one additive was used (ZrO_2) to improve the densification and microstructure with two bauxite containing bauxite containing batches.

CHAPTER 2
LITERATURE REVIEW

2. Literature Review

The high temperature transformation of sillimanite to elongated mullite crystals has been studied by **A. Tomba** et. al [1]. Sillimanite group minerals have the composition ($Al_2O_3.SiO_2$),can transform in to mullite and silica at temperatures between 1300°C and 1600°C depending on the polymorphic form. Sillimanite beneficiated mineral was cold isopressed at 200 MPa into cylindrical bars and then fired in air between 1500°C and 1650°C for 4h. From the microstructure and characteristic properties, it can be concluded that the larger part of the mullitization of sillimanite takes place in a temperature interval between 1550°C and 1650°C. At these temperatures, the transformation produces liquid and mullite. Elongated mullite grains with ahigh degree of orientation are always produced. A rapid nucleation occurs above a critical temperature, 1550°C, due to the resemblance of sillimanite and mullite structures. Below 1500°C, there is no evidence of sillimanite-mullite transformation. The critical temperature (1550°C) of sillimanite to mullite transformation was not modified by presence of liquid phase due to the minor impurities in the starting material. Finally, a step of acid leaching was employed to remove the glassy phase and high-grade purity mullite powders were obtained.

Ibram Ganesh et. al [2] found that dense mullite aggregates with 60% and 70% Al_2O_3 can be prepared from precursor mixtures consisting of beach sand sillimanite and a high-purity aluminium hydroxide following conventional single-stage and double-stage firing processes. The bulk density, apparent porosity, and water absorption capacity of sintered mullite aggregates were found to bestrongly influenced by the premullitization step of this precursor mixture. The premullitization step of precursor mixtures followed by a milling process enhanced the phase transformation into mullite and densification, enabling one to obtain 100% mullite phase aggregates denser than the current commercial products in a double-stage firing process(1250°C, 1 h + 1550°C, 1 h).Mullite aggregates formed in a double-stage firing process exhibited higher BD and mullite content and lower APand WA capacity in comparison with those obtained by the single-stage firing process.

H.S. Tripathiet. al [3] discussed the Mullite development by reaction sintering of sillimanite beach sand and calcined alumina. In the test, batches were prepared with the sillimanite beach

sand as well as by the addition of calcined Al_2O_3 to convert the SiO_2 available into mullite Sintered products thus obtained were characterized in terms of bulk density, apparent porosity, mechanical and thermo-mechanical properties and microstructure. The result showed that highest bulk density 3.04gm/cc is achieved. Alumina addition always lower the hot MOR at 1200°C due to the reduction of high silica glass content. Higher amount of impurities containing sand densifies at lower temperature through liquid phase sintering. X-ray diffraction pattern of some sintered samples are showed that the main crystalline phase present is mullite.Mullite formed in the samples retains the orthorhombic habit of sillimanite. Mullite crystals are interlocked with each other. Small amount of rounded to sub rounded ZrO_2 embedded in the mullite matrix is also noticed. ZrO_2 reduces the grain growth of the mullite which isformed in situ.

Microstructure and properties of sintered mullite developed from Indian bauxite studied by **H.S. Tripathi** et. al [4]. Dense mullite aggregates with 72% Al_2O_3 have been synthesized by reaction sintering of two varieties of Indian bauxite and silica sol. The bauxites used are of inferior grade with different levels of accessory impurities such as Fe_2O_3, TiO_2, CaO. The phase and microstructure development of sintered samples were investigated by XRD and SEM. Mullite formed from low impurity bauxite is mostly equiaxed, whereas mullite developed from bauxite with higher impurity particularly CaO is needle shaped. At1050°C the initial peaks of mullite appear and the nature of the peaks shows that the initial mullitization has started. It was found that the bulk density gradually increases with sintering temperature up to 1600°C followed by decrease indensity at 1650°C. Gradual removal of open pores with anincrease in sintering temperature is the reason for higher densification.

Thermo-mechanical properties of mullite–zirconia composites derived from reaction sintering of zircon and sillimanite beach sand: Effect of CaO has been studied byP. KUMAR et. al[5]. Mullite–zirconia composites containing 20% zirconia (mass fraction) were prepared by reaction sintering route utilizing Indian coastal zircon flour and sillimanite beach sand. 4%−12% of CaO (mole fraction) with respect to zirconia was used as additive. The effect of additive ondensification, microstructure as well as various mechanical and thermo-mechanical properties was studied. Incorporation of CaO reduced the densification temperature of the composites to 1550 °C compared to 1600 °C (for CaO freesamples). CaO formed small amount of liquid phase

(calcium aluminosilicate), which facilitated sintering. Average grain size of thecomposites decreased up to 4% CaO addition, afterwards grain size increased with further addition of CaO. Samples with 4% CaO exhibited ~225 MPa of flexural strength, ~6 MPa·m1/2 of fracture toughness and significant improvement in thermal shock resistance. CaO stabilized the tetragonal zirconia phase and thus improved the mechanical properties. Also, CaO stabilized the tetragonal zirconia phase and improved the thermal shock resistance. Samples with 4% CaO retained around 64% of its initial flexural strength even after 15 thermal shock cycles.

S. Rahman et. al **[6]** discussed the Structure description of the thermic phase transformation of sillimanite–mullite. The thermic phase transformation of sillimanite to 3:2 mullite was structurally examined with the main focus on the initial stageof this transformation. Single crystals of very pure sillimanite were annealed for different time periods (1600°C; 45 min–96 h) and then analysed employing X-ray and electron microscopic investigations. Using the videographic reconstruction method, the initial stage of the transformation (2–6 h, 1600°C) of sillimanite to 3:2 mullite is characterized as follows: (1) Splittingof the oxygen sites, resulting in tetrahedra- and octahedra-tilts and/or rotations; (2) statistical distribution of Si and Al on the tetrahedral sites. The results of the videographic reconstruction were confirmed via videographic simulations. A prolonged period of thermal treatment (24 h,1600°C) leads to the complete transformation of sillimanite to 3:2 mullite with precipitations of amorphous SiO_2.

Synthesis and thermo-mechanical properties of mullite–alumina composite derived from sillimanite beach sand: Effect of ZrO_2 studied by **H.S. Tripathi** et. al **[7]**. The raw materials and additive were mixed,attrition milled and sintered in compacted form at 1400–1600°C with 2 h soaking. Then the effect of ZrO_2 on the densification behaviour,thermo-mechanical properties and microstructure wasstudied.It was found that addition of ZrO_2 slightly retards the densification process. All the samples achieved their highest bulk density at 1600°C. X-ray diffraction pattern showed the major crystalline phase was mullite with some amount of corundum. A small amount of zirconia both in monoclinic and tetragonal form was also noticed. Scanning electron micrography shows that ZrO_2 occupies both an intergranular and intragranular position in the mullite matrix. The mullite formed at 1600°C ismostly equiaxed in nature that

suggests densification mainly occurs through solid state sintering.Thermo-mechanical properties of the sintered samples are not effectively altered by the presence of ZrO_2. ZrO_2containing samples always show better resistance to thermal shock than the ZrO_2 free samples. Mullite formed is non stoichiometric in nature and maximum solid solubility of ZrO_2 withinthe mullite structure is 1.70 wt.%

Sasmita Prustyet. al [8] investigate the effect of MgO additive on the structural, microstructural and hardness properties of zirconia mullite (MUZ). The MgO additive in MUZ not only stabilizes the cubic zirconia phase but also acts as a sintering aid for the formation of cross-linked mullite grains. The micrograph of plasma sintered composites shows a ladder like structure and a complete cross-linked mullite grains whereasthe surface morphology of conventionally sintered composites clearly indicates the presence of small and big grains close packed to each other. From the X-ray diffraction and Fourier transform infrared studies, it has been realized that complete dissociation of sillimanite andzircon has been occurred for the conversion of zirconia/mullite aggregates in plasma fused MgO–MUZ composites within the5 min of plasma arching. Uniform arrangement of mullite platelets and dendritic structure of zirconia has been observed in the surface of plasma fused MgO–MUZ composites whereas ladder like structure with complete interconnected mullite grains has been observed for plasma sintered composites. Appreciable hardness and higher optical band gap have been observed for plasma fused MgO–MUZcomposites. The total sillimanite and zircon mixtures have been utilized for the complete conversion of mullite and zirconia composites in plasma fusion whereas the complete conversion of sillimanite and zircon has not observed in plasma sintered and conventionally sintered composites.

Preparation and properties of Y_2O_3 containing zirconia–mullite composites derived from sillimanite beach sand discussed by**Manas K. Haldar** et. al [9].All raw materials have been attrition milled and then isostatically pressed followed by sintering in the range of1500–1600°C with a 2-h soaking period. Then the sintered materials have been characterised in terms of bulk density, linear shrinkage, hot modulus of rupture, X-ray diffraction, infrared spectroscopy and microstructural features. The addition of yttrium oxide overall improves the physical, thermo-mechanical properties of the composites. As the sintering temperature increases, yttrium oxide

helps in grain growth of the samples. Exaggerated grain growth is responsible for higher porosity as the temperature increases. But the samples without additive show a down trend in porosity with rise in temperature. The microstructure of zirconia-mullite composites are characterized by of elongated mullite grains along with sub rounded to rounded zirconia grains. There are two types of zirconia particles present in the microstructures. One is intergranular and other one is intragranular. The microstructurecontains elongated and equiaxed mullite grains (black) along with zirconia grains (white). Most of zirconia grains are intergranular and few are intragranular.

Sintering of Mullite-Containing Materials: Effect of Composition found by **D. Sackset**. al [10] found the Sintering behaviour of mullite-containing powdersover a range of chemical compositions (Al_2O_3/SiO_2 ratio). Densification measurements were made for both liquid phase-containing and solid-state systems. Small amounts ofliquid phase were observed to have a significant effect ondensification rate. A linear relation was obtained between thepercent of theoretical density and the logarithm of time for compositions in the range 73 to 75 wt.% Al_2O_3.Grain-boundary transport or diffusion appeared to be the primary mechanism of densification. A glass phase, however, persistedup to 74 wt.% Al_2O_3, presumably because of metastable behaviourdriven by a lowering of high mullite-mullite interfacial energies. A sharp decrease in densification rate was observed on transitionfrom the mullite solid solution range to the mullite and alumina phase region. This decrease was associated with elimination of theresidual glassy phase.

G.Orangeet. al [11] studiedthe mechanical behaviour of reaction-sinteredmullite/zirconia composites (RSMZ) at room temperature and up to1200°C. It is well established that fully densefine-grain mullite/zirconia or mullite/alumina/zirconia composites with enhanced mechanical properties can be produced by reaction-sintering routes. These materials, obtained with a low-cost process have potential usesas structural ceramics up to at least 1000°C.It appears that published toughening mechanisms cannot explain by themselves the mechanical properties of these composites. The needle-like morphology of mullite grainsleads to a lengthening ofthe fracture path and a higher proportion oftrans granular fracture mode.Thermal shock resistance has also been determined. It wasfound that dispersion of zirconia particles and the particular microstructure of mulliteobtained by means of an insitu reaction process leads to improved

properties, with aroom temperature fracture toughness of about 5.25 MPa m 1/2. Up to 1000°C fracturestrength and toughness values are quite high, which make these materials potential candidates for high temperature applications.

Controllable preparation and synthetic mechanism of mullite from the bauxite with Fe-rich oxide content studied by **Mingwei Yan**et. al [12].In this paper, controllable preparation of mullite was attained using the bauxite with Fe-rich oxide content as raw materials, by adjusting its mass ratio of $(Fe_2O_3+Al_2O_3)/SiO_2$ to about 2.57 based on the theoretical design of Fe_2O_3-Al_2O_3 binary diagram and $Al2O_3$-SiO_2-TiO_2 ternary diagram. Phase and synthetic mechanism of mullitefrom the Fe-rich bauxite have been characterized and analysed by XRD, SEM, EDS. Crystal phases of the bauxite with Fe-rich oxide content after sintering are composed of mullite solid solution, aluminium titantate solid solution and cristobalite with aluminium titantate solid solution distributed dispersively and surrounded by mullite solid solution. The synthetic mechanism of mullite solid solution can be expressed as follow: in the sintering process of the bauxite with mid-low grade, mullite is firstly formed by mullitization behaviour, and then Fe^{3+} and Ti^{4+} ions occupy and replace Al^{3+} located in the octahedral or tetrahedral sites for mullite. Si^{4+} in the tetrahedral site will be simultaneously substituted by Al^{3+} to maintain electrovalenc eequilibrium. As a result, mullite solid solution containing Fe^{3+} and Ti^{4+} is eventually developed. A very little of amorphous phase exists between mullite crystals, and aluminium titantate solid solution is distributed dispersively and surrounded by mullite solid solution.

Correlation between properties of zirconia mullite and Y_2O_3 stabilised zirconia mullite derived by various processing techniques described by **S. Prusty** et. al [13]. Zirconia mullite (MUZ) and Y_2O_3–MUZ composites were synthesised by plasma melting, plasma sintering and conventional sintering techniques. Mixtures of tetragonal and cubic phases have been observed in all the processed Y_2O_3–MUZ composites. The XRD and micro-Raman studies indicate that the addition of Y_2O_3 in MUZ transforms the monoclinic zirconia to cubic zirconia phase. The optical absorption studies completely reflect the improvement in optical band gap of Y_2O_3–MUZ composites to prove it as a suitable candidate for refractory applications. The bulk density,hardness and higher crystalline nature of plasma sintered composites indicate that better products can be synthesised by direct current extended arc thermal plasma heating technique

within a short duration of time. In conclusion, their correlation studies on the properties of MUZ and Y_2O_3–MUZ open an avenue to determine the appropriate melting and sintering procedures for enhancing the physical properties of the materials as desired for industrial applications.

Manas K. Haldar et. al [14] found the effect of magnesia additions on the properties of zirconia–mullite composites derived from sillimanite beach sand. Zirconia–mullite composites with 4–8 mol% magnesium oxide has been prepared from Indian coastal sillimanite beach sand, zirconia and alumina. The X-ray diffraction study reveals that in zirconia, monoclinic is the major phase, Alumina is having α-Al_2O_3 as main constituent & in magnesia periclase is the major phase. Milling of the mixtures of all raw materials has been carried out in an attritor mill for 9 h. After drying and pressing the samples were sintered between 1500°C and 1600°C with 2 hrs of soaking. The physical, mechanical & thermo-mechanical properties of the sintered materials namely bulk density, linear shrinkage, hot modulus of rupture, hardness and fracture toughness have been evaluated. The infra-red spectrums of sillimanite sand and sintered samples have been described. The bulk density of the sintered samples falls with increase in temperature with varying amount of magnesia. The linear shrinkage of the sintered samples increases with higher content of magnesia. The hot modulus of rupture for all samples is showing lower value at 1600°C. The sintered materials are having higher value of fracture toughness than puremullite. All the sintered composites are showing an overall decreasing trend in modulus of elasticity as the sintering temperature increases. The scanning electron microstructures of the sintered samples show bright zirconia grains are uniformly distributed throughout the darker mullite matrix.

High-temperature characterization of reaction-sintered mullite-zirconia composites discussed by **Philippe Descamps** et. al [15]. Mullite-zirconia composites are prepared by reaction sintering of zircon and alumina, either using reaction and sintering additives (Titania (T-MZ) or Magnesia (M-MZ)) or starting from highly reactive powder mixtures obtained by an ultra-rapid-quenching technique (URQ-MZ). In the latter case, the presence of large amounts of an amorphous phase in the quenched powders enables sintering without the use of additives. The various composites differ mainly by their microstructure-i.e., the mullite grains aspect ratio and grain size-and by the quantity and nature of impurities or additives. Within this work, the modulus of rupture and

critical stress intensity factor of each material are measured from room temperature to 1200°C. Bending creep is also investigated for various temperature and stress ranges. For the three materials, the fracture toughnessdecreases with temperature, according to tetragonal zirconia stabilization, up to 600°C to 700°C, above which a significant increase occurs. The reinforcement is more efficient for T-MZ because of the higher viscosity of the glassy phase. Despite its larger amount of glassy phase, the M-MZ ceramic shows the better creep resistance because of its particular microstructure consisting of cross-linked elongated mullite grains-which impedes grain-boundary sliding.

Manas K. Haldar et. al [16] found that Zirconia–mullite composites can be prepared from beach sand sillimanite in the presence of magnesia as an additive. The raw materials were attrition milled. Samples were isostatically pressed and sintered in the temperature range of 1500–1600°C with 2hr of soaking. The resulting composites were characterized in terms of densification, thermal expansion, martensite start (Ms) temperature. The presence of magnesia changes the value of thermal expansion coefficient. The mechanical and thermo-mechanical properties, namely flexural strength and thermal spalling of the sintered composites, were characterized and effect of magnesia on it is discussed. The interrelation between microstructure and properties of a material is very important for greater understanding of material property and possibility of improvement. Zirconia has higher atomic number compared to aluminium and silica. So, it appears clearly from its surrounding mullite matrix under SEM and shows a brighter image (white). The EDAX analyses of zirconia, mullite and zirconia–mullite grain boundary showed that the mullite phase contains around 72% Al2O3 and 27% SiO2, whereas zirconia phase contains 90% ZrO2. A small amount of magnesia of 0.37% in mullite and 0.12% in zirconia is present. The most of magnesia (around 2.35%) is present in the zirconia–mullite grain boundary. Both zirconia and mullite contain a small amount of TiO2, which comes from raw material.

Mechanical properties of mullite–corundum composites prepared from bauxite having considerable amount of impurities and silica sol has been studied by **Atul V. Maldhure** et. al [17]. The effect of changing mullite phase proportion on the mechanical properties (i.e., flexural

strength, elastic modulus, hot modulus of rupture, thermal shock resistance) of prepared composites has been studied. Flexural strength and elastic modulus increase with increasing free corundum phase content in the composites. Hot modulus of rupture for the sample containing only mullite phase increases with increasing test temperature over entire temperature range. Only mullite/highest mullite phase proportion showed the highest resistance to both crack initiation and propagation. The values of these parameters decrease with increasing corundum phase proportion in the composites. Retention of mechanical strength after successive thermal shock cycles decreases with increasing corundum phase proportion in the composites. The reason for such behaviour is two fold, the thermal expansion mismatch between individual mullite and corundum phases, and increase in amount of glassy phase due to high impurity phase. The refractory composites containing only mullite showed the greatest performance in terms of high-temperature mechanical strength, loss of strength on thermal shocking, and ability of a material to resist crack propagation and further damage.

Effect of the calcining temperatures of low-grade bauxite on the mechanical property of mullite ceramics without any other additives discussed by **Qiang Ren** et. al [18]. The variations in physical and chemical properties in the process of sintering, the specific surface area of calcined bauxite at different calcining temperatures, and the phase composition of the mullite ceramic and its microstructure were investigated by thermal analysis, laser particle analysis, the X-ray diffraction, and scanning electron microscope, respectively. The mechanical properties of mullite ceramics prepared by calcined bauxite are superior to the properties of mullite ceramics made by raw bauxite, and the flexural strength of mullite ceramics improved with the increase of calcining temperatures at the range of 650-1200°C. The influence of calcining temperature of raw bauxite on the mechanism of sintering of mullite ceramics is reflected in these aspects, (i) the crystalline moisture andother impurities; (ii) the specific surface area of calcined bauxite powders; (iii) crystals in calcined bauxite. Using calcined bauxite to produce mullite ceramic was an applicable way, at the same time, this provides the application of low-grade bauxite for new thoughts. The deeper studies needed to be done before the research achievements areapplied to manufacture effectively.

Preparation of low-cost mullite ceramics from natural bauxite and industrial waste fly ash studied by **Yingchao Dong** et. al [19]. The fired samples, including fly ash, bauxite and their mixture based on the composition of 3:2 mullite, were characterized respectively by XRD (X-ray diffraction). The results indicate that the secondary mullitization occurred by the solid-state reaction of cristobalite and corundum below 1300℃, followed by the dissolution of corundum into transitory glassy phase at higher temperatures. The dilatometric results reveal that the formation of secondary mullite resulted in aslight expansion in spite of the shrinkage induced by sintering. In addition, the samples were fired at elevated temperatures and then characterized in terms of relative density, porosity, micro-structure and fracture strength. At 1600℃, the relative density and fracture strength are 93.94% and 186.19MPa, respectively. After sintering at 1600℃ for 4 h, the sample exhibiteda closed porosity of 5.44% and open porosity of 0.62%. Itis crucial to prepare denser mullite ceramics by avoiding the formation of closed pores. The development of mullite ceramics would add great economic value to industrial waste fly ash that existed abundantly throughout the world, most of which are not well utilized currently. Moreover, inexpensive raw natural mineral bauxite was testified as an effective substitute for industrial alumina for the production of mullite. This fact supports the practicability of thedirect use of natural raw materials, instead of alumina producedby the complicated process.

Toshiyuki Koyamaet. al [20] found that Mullite-zirconia composites can be prepared from three kinds of combination of starting materials such as mullite-zirconia (MM), alumina-silica-zirconia (RS3) and alumina-zircon (RS2). Phase formation reaction, sinterability and microstructures of these samples were investigated. The following conclusions can be drawn.

(1) The mixture of mullite and zirconia powders(MM): Sinterability of this sample was notso good compared with the others. At highertemperature, it released silica from mullite and formed a liquid phase, which caused the growth of elongated large mullite grains inthe microstructure.

(2) The mixture of alumina, amorphous silica and zirconia powders (RS3): Sinterability ofthis sample was good because of the enhancement of densification by a viscous flow mechanism due to amorphous silica phase. Equiaxed mullite grains and intergranulary dispersed zirconia grains formed the microstructure.

(3) The mixture of alumina and zircon (RS2): Extremely alumina-rich mullite were formed transiently in this sample. Their microstructures were composed of irregularly shaped mullite

and intra/intergranularly dispersed zirconia grains. Some extent of Zr atoms was considered to be incorporated in the transient state mullite.

H.S. Tripathi et. al [21] discussed the Sintered mullite from aluminous ore for refractory application. Mullite aggregate was prepared by reaction sintered from Aluminous ore with calcined alumina and added Titania to enhance the densification process without deterioration of thermo-mechanical properties. The major raw materials used in this investigation were kyanitic aluminous ore and Bayer's alumina. Batches were mixed and milled in a vibroenergy mill 8 h. Then rectangular bars were uniaxially pressed at 100 MPa and sintered in air at 1500, 1550, 1600 and 1650°C with 2 h soaking time. Sintered products thus obtained were characterized in terms of bulk density, apparent porosity, high-temperature flexural strength and microstructure. So, results showed that at 1600°C, 1 wt.% TiO_2 addition decreases the porosity from 2.2 to 0.5%. An XRD pattern of the mullite aggregate developed at 1600°C shows that the main crystalline phase is mullite,with a small amount corundum.A SEM photomicrograph of the same sample shows that the mullite grain developed from kyanite. Aluminous materials are mostly acicular in shape and the glassy phase is evenly distributed in the intergranular position. Some equiaxed mullite grains smaller in size also are observed. Flexural strength at 1300°C of the mullite aggregate developed at 1600°C shows that mullite with no additive exhibits the highest flexural strength of 73.5 MPa at 1300°C.Beyond 1 wt.% TiO2 addition, the decrease in strength is not appreciable (up to 3 wt.% TiO_2). Because TiO_2 forms solid solution with mullite, it does not significantly alter the amount of glassy phase or glass composition.

Structure and properties of mullite discussed by **H. Schneider** et. al [22]. Mullite has achieved outstanding importance as a material for both traditional and advanced ceramics because of its favourable thermal and mechanical properties. Depending on the synthesis temperature and atmosphere mullite is able to incorporate a number of transition metal cations and other foreign atoms. In more detail: Parallel to **a** the tetrahedra are linked to the relatively short stiffer Al–O (A, B) bonds, whereas parallel **b** they are linked parallel to the relatively long more compliant Al–O(D) bonds. In mullite some of the oxygen atoms bridging the tetrahedra are removed for charge compensation. This gives rise to the formation of oxygen vacancies and of T_3O groups (so-called tetrahedral triclusters). The anisotropy of the bonding system of mullite has a major

influence on the anisotropy of its physical properties. Heat capacity and thermal expansion measurements of mullite display reversible anomalies in the temperature range between about 1000 and 1200°C. It is believed that tetrahedral cations, bridging O atoms, and O vacancies undergo dynamical site exchange processes at high temperatures. At lower temperatures the dynamic disorder may transform to a static one. Diffraction experiments revealed that also partially ordered states may exist.

Thermo-mechanical properties of mullite/zirconia reinforced alumina ceramic composites investigate by **M.M.S. Wahsh** et. al [23]. Alumina–mullite–zirconia ceramic composites was prepared by reaction bonding of alumina and zirconmixtures after firing at differenttemperatures 1300°C, 1400°C and 1500°C. Constant amount of magnesia was added as a sintering aid. The technological parameters of the sintered ceramic composites, i.e. the mechanical properties and densification parameter as well as thermal shock resistance, have been investigated. The main phases in all samples fired at 1500°C are corundum (α-Al_2O_3), monoclinic zirconia (m-ZrO_2) and tetragonal zirconia (t-ZrO_2). In addition, some diffraction peaks of mullite ($3Al_2O_3.2SiO_2$) and magnesium-aluminium-silicate ($Mg_{3.5}Al_9Si_{1.5}O_{20}$; Sapphirine) were detected in samples containing higher amounts of zircon. All ceramic composites achieved an excellent thermal shock resistance (TSR). Ceramic composite containing 66.79 mass% calcined alumina, 30.52 mass% zircon and2.69 mass% magnesia fired at 1500°C exhibited higher densificationparameter (BD~3.31 g/cm3, AP~5.5%) and mechanical properties (CCS~550 MPa) as well as excellent thermal shock resistance. This alumina–mullite zirconia ceramic composite can be suggested for using in refractory and high temperature applications where severe thermal shock and high mechanical properties are required.

Cemail Aksel et. al [24] described the role of fine alumina and mullite particles on the thermo-mechanical behaviour of alumina–mullite refractory materials. Fine grain alumina and mullite particles were incorporated into slip-cast alumina–mullite refractories in order to investigate their effects on the microstructure, mechanical properties and thermal shock behaviour of the refractories. The addition of fine mullite resulted in ahigh porosity and low mechanical properties, both densification and mechanical properties increased with the incorporation of fine alumina particles significantly through improvement of interparticle bond strength amongst the

coarser grains. Therefore, more fracture surface energy was required to connect the cracks for propagation, associated with a high value of fracture toughness. The strength and Young's modulus were also improved with increasing quench temperature, leading to a high thermal shock resistance. Furthermore, the crack initiation resistance was also increased with higher alumina content. Thermal shock tests confirmed that the addition of fine alumina rather than fine mullite particles into an alumina–mullite slip-cast refractory material improved both strength and modulus values with increasing quench temperature, indicating better thermal shock resistance.

H. Schneider et. al [25] studied the temperature dependent solubility of titanium, iron, and magnesium in mullites coexisting with SiO_2-rich partial melts in a used chamotte brick was studied with a high-resolving microprobe. The mullites of the starting material have relatively high mean Fe203 (~ 2.4 wt.%), but lower TiO2 (~ 1.4 wt.%), and very low MgO contents (~0-5wt.%). Cation removal from mullite to coexisting glass phase is observed at high temperature: the onset of exsolution is about 1300°C for magnesium, 1350°C for iron, and 1400°C for titanium. Sample specimens annealed at 1650°C have mullites with about 0-5 wt.% Fe_2O_3, 0.9wt.% TiO_2, and traces of MgO. Cation exsolution curves follow exponential laws, the exsolution rate being considerably higher for Fe_2O_3 than for TiO_2 and MgO. The study documents amuch higher mobility of the iron ion as compared to that of titanium. Eutectic melting of mullite with associated limited solid solution of iron, titanium, and magnesium cannot be the only reason for cation removal from mullite to the coexisting melt because the amount of mullite dissolution between 1300 and 1650°C is too low. A cation distribution between mullite and coexisting melt, the value of which decreases with temperature is believed to be a further driving force for cation exsolution.

.

CHAPTER 3

PLAN OF THE WORK

3.Plan of the Work:

The present work was performed to study the effect of bauxite on the mullitization and densification of sillimanite. The effect of zirconia addition on the bauxite-sillimanite mixture was also studied.

For this purpose, Indian sillimanite beach sand (Kerala) and Saurashtra bauxite were selected. The physio-chemical characteristics of the principle raw materials were studied through chemical analysis, phase analysis by powder XRD, Differential thermal analysis and specific gravity measurement.

The batch compositions were selected, and thoroughly mixed & ground and then calcined at appropriate temperature to get reactive powder. Sintering study was reformed on small discs. The green samples after proper drying were subjected to firing. The firing was done in oxidising atmosphere.

The sintered compact bodies were characterised with respect to the variables through the determination of some physical properties. These included bulk density, apparent porosity, diameter, shrinkage etc. the different crystalline phases developed in the sintered body were examined by powder X-ray diffraction study.

The properties of sintered products depend on the microstructure developed in the body that means the nature and distribution of different phases. A thorough investigation on the densification of different phases, their morphology and their size were determined by examining the chemically etched fractured surface. The approximate chemical composition of the different crystalline and amorphous phase developed were estimated by energy dispersive x-ray analysis (EDX). The study this microstructural analysis will help to understand its relation with other physio-chemical and thermo-chemical properties.

For refractory application, cold crushing strength, chemical corrosion and pyrometric cone equivalent tests are also measured

CHAPTER 4

EXPERIMENTAL WORK

4. Experimental Work

At first raw materials, Sillimanite fine (-300 mesh), Bauxite (supplied by Shri Nataraj Ceramic & Chemicals Industries Ltd, Gujarat), Zirconium Dioxide (LOBA CHEMIE) were used for the study. The main raw materials were characterized by chemical analysis, phase identification by powder XRD, specific gravity measurement and differential thermal analysis (DTA). Bauxite was ground in a rubber lined pot with alumina as grinding media for 5 hours. The slurry from the pot mill was dried at 110ºC±5ºC. The batch composition and the sample codes of different batches are listed in **Table 1**.

Table 1: Batch Composition and batch code for the stage-I

Batch code	Sillimanite	Bauxite
SB0	100	0
SB2	80	20
SB3	70	30
SB4	60	40
SB5	50	50

Each batch was thoroughly mixed in a plastic container with small alumina ball for 45 mins. After that mixed batch was calcined at $600^{\circ}C$ for 2 hrs. The batch powder was mixed with 5% PVA and granulated through 30 BS sieve. The granulated materials were pressed at 120MPa into 20mm and 25mm diameter discs, dried at 110ºC and fired at 1500º to 1650ºC with 2hr soaking time. Bauxite was added in 20, 30, 40 and 50wt% to the mixture.
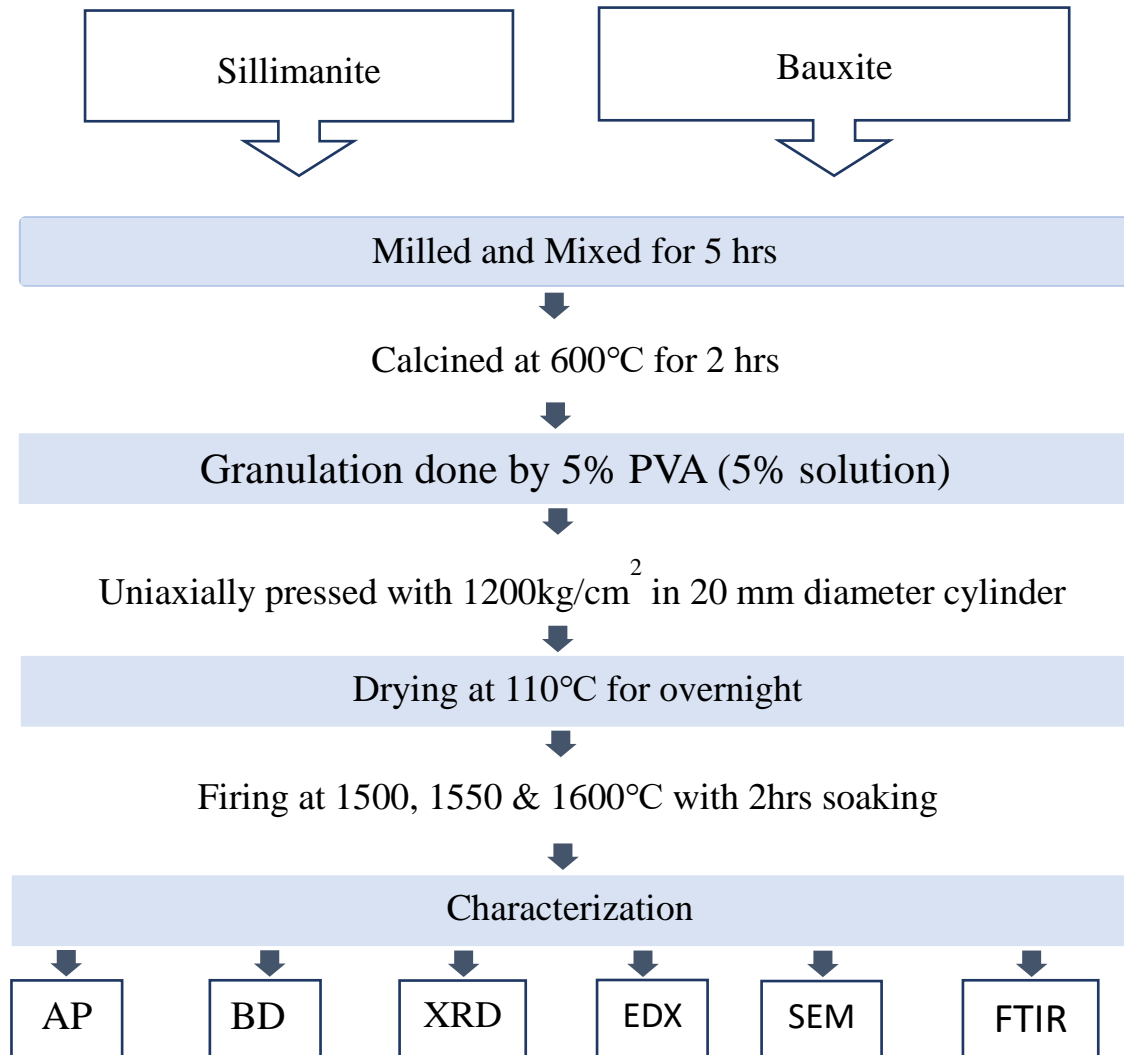
After that from the optimized batches, we have taken two batches and add zirconium dioxide in stage-II. Zirconia was added in 1, 3 and 5wt% to the mixture. The same mixing, calcining, granulation, pressing and firing were followed as in stage-I. The batch composition and the sample codes of different batches for stage-II are listed in **Table 2**.

Table 2: Batch Composition and batch code for the stage-II

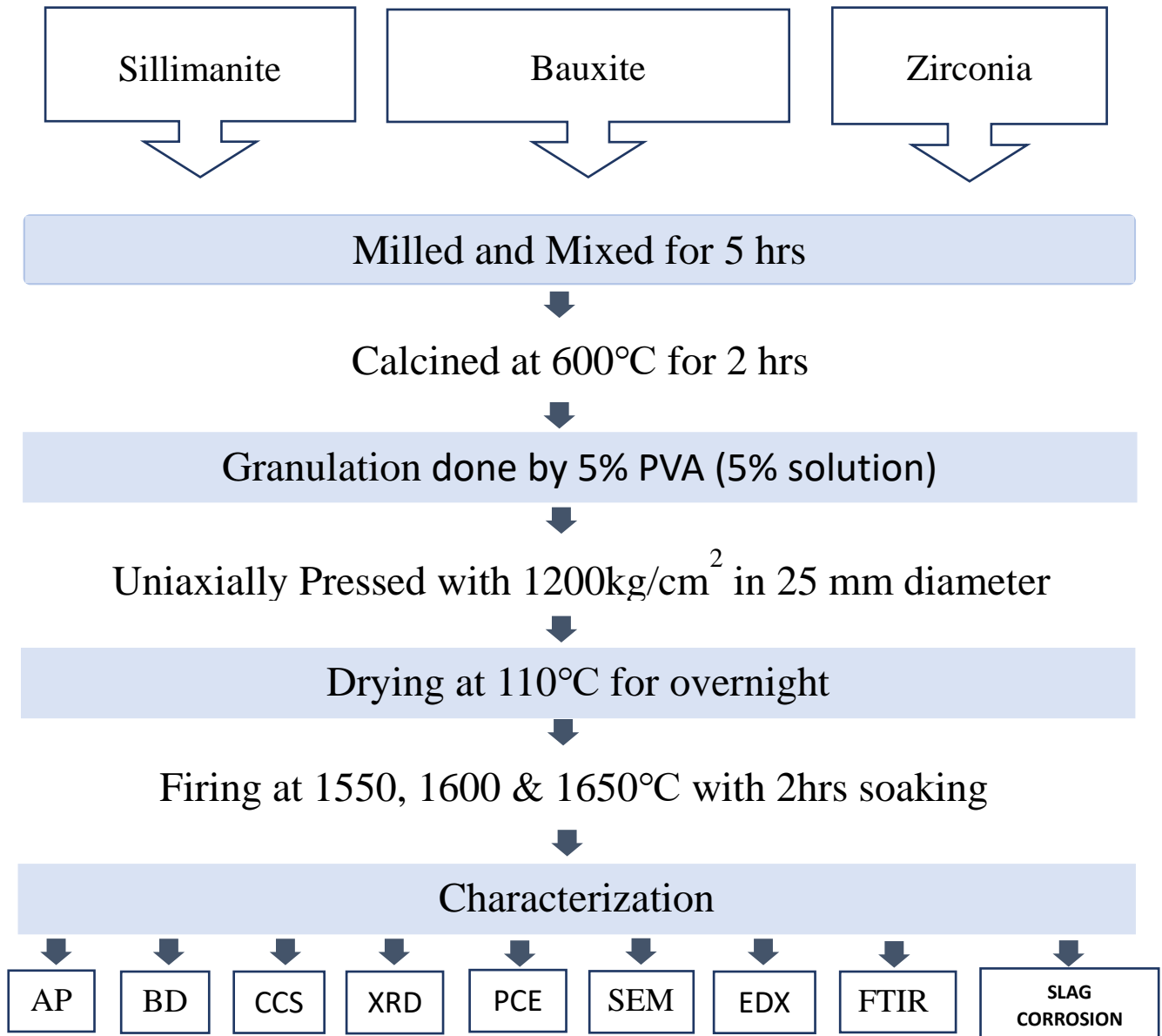| Batch code	Sillimanite	Bauxite	Zirconia	Batch code	Sillimanite	Bauxite	Zirconia
SB4-Z0	60	40	0	SB5-Z0	50	50	0
SB4-Z1	60	40	1	SB5-Z1	50	50	1
SB4-Z3	60	40	3	SB5-Z3	50	50	3
SB4-Z5	60	40	5	SB5-Z5	50	50	5

The process flow chart is given below-

Figure1: Process flow chartfor the stage-I

Sillimanite

Bauxite

Milled and Mixed for 5 hrs

Calcined at 600°C for 2 hrs

Granulation done by 5% PVA (5% solution)

Uniaxially pressed with 1200kg/cm^2 in 20 mm diameter cylinder

Drying at 110°C for overnight

Firing at 1500, 1550 & 1600°C with 2hrs soaking

Characterization

AP   BD   XRD   EDX   SEM   FTIR

The process flow chart for stage two is given below-

Figure 2: Process flow chart for the stage-II

Sillimanite	Bauxite	Zirconia

Milled and Mixed for 5 hrs

Calcined at 600°C for 2 hrs

Granulation done by 5% PVA (5% solution)

Uniaxially Pressed with 1200kg/cm^2 in 25 mm diameter

Drying at 110°C for overnight

Firing at 1550, 1600 & 1650°C with 2hrs soaking

Characterization

AP	BD	CCS	XRD	PCE	SEM	EDX	FTIR	SLAG CORROSION

4.1 Characterization of Raw Materials

The following physical and thermal tests was conducted for the raw materials, Saurashtra Bauxite and Kerala Sillimanite.

a) Specific gravity (ρ)
b) X-ray Diffraction (XRD)
c) Differential Thermal Analysis (DTA)
d) Fourier-transform infrared spectroscopy (FTIR)

a) Specific gravity

Specific gravity, also referred to as relative density, is used to relate the weight or density of liquids to that of water. Specificgravity is the ratio of the mass of a substance to the mass of a reference substance for the same given volume. *Apparent* specific gravity is the ratio of the weight of a volume of the substance to the weight of an equal volume of the reference substance. Here we measure the sp. Gravity by pycnometer. A pycnometer allows measuring the volume and the density of solid objects in a non-destructive manner. The latter is accomplished by employing Archimedes' principle of fluid displacement for liquid pycnometer.

The specific gravity of sample is determined using the relation:

$$G = \frac{M_2 - M_1}{(M_2 - M_1) - (M_3 - M_4)}$$

Where, M_1 = mass of empty Pycnometer.
M_2 = mass of the Pycnometer with dry sample.
M_3 = mass of the Pycnometer and sample and xylene.
M_4 = mass of Pycnometer filled with xylene only.
G = Specific gravity of sample.

b) X-ray Diffraction(XRD) analysis

A scattering of X-ray by the atom of a crystal that produces an interference effect so the diffraction pattern gives information o the structure of the crystal or the identity of a crystalline substance.

The objective of XRD is to know the composition of a crystalline material, which helps to determine different properties of that substance.

Selected sample was crushed into iron mortar and pestle, passed through 30 mesh B.S. demagnetized and finely ground (much below 200 mesh) in anagate.

The nearly 3gm sample is required.

Bragg's law is employed.

The instrument uses Ni-filtered Cu K_a radiation with a scanning rate of 2° per minute. The data had to be either compared using monographs already collected or using software crystalline phases are detected.

They were finally plotted neatly using ORIGIN software.

c) Differential Thermal Analysis (DTA)

It is a thermo-analytic technique that is similar to differential scanning calorimetry. In DTA, the material under study and an inert reference are made to undergo identical thermal cycles, (i.e., same cooling or heating programme) while recording any temperature difference between sample and reference.This differential temperature is then plotted against time, or against temperature (DTA curve, or thermogram). Changes in the sample, either exothermic or endothermic, can be detected relative to the inert reference. Thus, a DTA curve provides data on the transformations that have occurred, such as glass transitions, crystallization, melting and sublimation. The area under a DTA peak is the enthalpy change and is not affected by the heat capacity of the sample.

A DTA consists of a sample holder, thermocouples, sample containers and a ceramic or metallic block; a furnace; a temperature programmer; and a recording system. The key feature is the existence of two thermocouples connected to a voltmeter. One thermocouple is placed in an inert material such as Al_2O_3, while the other is placed in a sample of the material under study. As the temperature is increased, there will be a brief deflection of the voltmeter if the sample is undergoing a phase transition. This occurs because the input of heat will raise the temperature of the inert substance, but be incorporated as latent heat in the material changing phase.

d) Fourier-transform infrared spectroscopy (FTIR)

A technique used to obtain an infrared spectrum of absorption or emission of a solid, liquid or gas. An FTIR spectrometer simultaneously collects high-spectral-resolution data over a wide spectral range. This confers a significant advantage over a dispersive spectrometer, which measures intensity over a narrow range of wavelengths at a time.

Firstly, The KBr thin platesare prepared and scanned in FTIR machine. Then, the powder sample and KBr are mixed together and thin plates are prepared. These plates are scanned in FTIR machine. Final result is analysis with paper.

4.2Analysis of Sintered Material

a) Apparent Porosity
b) Bulk Density
c) Shrinkage
d) Scanning Electron Microscopy
e) Energy Dispersive X-ray Analysis
f) Slag Corrosion
g) Fourier-transform infrared spectroscopy
h) X-ray Diffraction

a) Apparent Porosity (AP)

Apparent porosity is defined as the ratio of the volume of the open pores to the bulk volume of the material. It is expressed as a percentage.

The test specimenare taken. Then, such test pieces are tied with a thread and is thereby hanged from the test rod. Such a Glass rod containing the test specimen is placed inside the beaker containing water such that the test specimen suspended in water so that any part of it should not be touched with the walls or bottom of the beaker.

The whole assembled beaker is placed on heater at 110°C for 2hrs. So that the open pores in the piece are filled up with the water quickly. Then, the samples are placed in cold water for a few minutes to get it cooled and then, the test pieces are tied with a wire which hangs from the knot of the weight to get it cooled and then, the test piece is tied with a wire which hangs from the knot of the wight balance such that the test piece should remain completely immersed in the water in the beaker.

Thus dry weight (D), suspended weight (S) and soaked weight (W) is calculated for the test specimen. Dry weight (D) should be calculated by drying the test specimen for overnight.

Suspended weight (S) and soaked weight (W) is measured. The apparent porosity (AP) is then calculated by the following equation.

$$A.P. = \frac{W-D}{W-S} * 100 \ \%$$

b) Bulk Density

Bulk density is a property of powders, granules, and other "divided" solids, especially used in reference to mineral component (soil, gravel), chemical substances, (pharmaceutical) ingredients, foodstuff, or any other or particular matter. It is defined as the mass of many particles of the material divided by the total volume they occupy. The total volume includes particle volume, inter-particle void volume, and internal pore volume.

This method of determining bulk density is preferable for specimens which are branded deeply or are irregular in contour. It is more than the direct measurement method.

The dry weight (D), suspended weight (S) and soaked weight (W) is calculated for the test specimen. Dry weight (D) should be calculated by drying the specimen for overnight.

Suspended weight (S) and soaked weight Weight (W) are measured by water displacement method. Bulk density is calculated in gm/cm^3. The bulk density is given by the formula.

$$BD = \frac{D}{W-S} \ gm/cc$$

c) Shrinkage

The diameter of the samples was measured before firing (a) and after firing (b). Then it is calculated by ((b-a)/a)*100. It is calculated in percentage.

$$Shrinkage = \frac{b-a}{a} * 100 \%$$

d) Scanning Electron Microscopy (SEM)

A scanning electron microscope (SEM) is a type of electron microscope that produces an image of a sample by scanning it with a focused beam of electrons. The electrons with atoms in thesample, producing various signals that contain information about the samples surface topography and composition.

Samples were first broken into a thin plate.

Then samples were chemically etched. Chemical etching was carried out by treating the sample surface using 40vol% HF for 1min. The etched surface was washed by 1:1 water and rectified spirit mixture in a ultrasonic cleaner.

Sample is coated with the platinum nanoparticle to make the surface conductive. Then SEM pictures were taken and grain composition was found out by EDXA.

e) Energy Dispersive X-ray Analysis (EDX)

Energy-dispersive X-ray spectroscopy (EDS, EDX, EDXS or XEDS), sometimes called energy dispersive X-ray analysis (EDXA) or energy dispersive X-ray microanalysis (EDXMA), is an analytical technique used for the elemental analysis or chemical characterization of a sample. It relies on an interaction of some source of X-ray excitation and a sample. Its characterization capabilities are due in large part to the fundamental principle that each element has a unique atomic structure allowing a unique set of peaks on its electromagnetic emission spectrum.

EDS makes use of the X-ray spectrum emitted by a solid sample bombarded with a focused beam of electrons to obtain a localized chemical analysis. All elements from atomic number 4

(Be) to 92 (U) can be detected in principle, though not all instruments are equipped for 'light' elements ($Z < 10$). Qualitative analysis involves the identification of the lines in the spectrum and is fairly straight forward owing to the simplicity of X-ray spectra. Quantitative analysis (determination of the concentrations of the elements present) entails measuring line intensities for each element in the sample and for the same elements in calibration Standards of known composition.

e) **Slag Corrosion Test of Refractories**

Slag attack is particularly important. The structural strength of the refractory may be critically reduced by the solvent action of liquid slags. The slag attack on the refractories in contact may be in two ways: Corrosion - It is the wear and tear of refractories caused by a static chemical attack of slag.i.e. the process of breaking and washing away of refractory materials by molten slag.

First, we have prepared cylindrically shaped specimens having a diameter 25mm. Then we make 10mm hole at the center and Depth around 2/3rd of specimens. Fired the sample according to the schedule.

Now, the fired samples are 2/3 filled with BF slag and fired at 1450^{0}C for 2 Hrs. The corroded samples are cut into two pieces by the help of cutting machine. Then the diameter of the penetration of the samples are observed and measured by a vernier scale.

CHAPTER 5

RESULT & DISCUSSION

5. Results and discussion:

Stage-I

The physic-chemical properties of the sillimanite and bauxite are presented in **Table-3**. Impurities in sillimanite is relatively low which constituted of only 1.64 wt.% with respect to bauxite one (12.59wt. %). Specific gravity of sillimanite is 3.24 higher than that reported by Grimshaw (3.08). [26] Mole ratio of Alumina to silica ratio is 1:1.1 means silica rich sillimanite. The powder X-ray shows small peaks of quartz with main sillimanite phase. FTIR spectra of sillimanite shown in **fig 3**, shows the characteristics transmittance peak at of sillimanite $1185cm^{-1}$. [14] FTIR of SB4 and SB5 shows the absence of sillimanite characteristics transmittance peak at $1185cm^{-1}$, confirms the total decomposition of sillimanite at this temperature.

Table 3: Physio-chemical properties of raw materials

Composition	Sillimanite	Bauxite
Al_2O_3	59.46	58
SiO_2	38.9	5.4
TiO_2	0.36	1.56
Fe_2O_3	0.72	1.72
CaO	0.56	1.6
MgO	----	0.1
P_2O_5	-----	1.0
Na_2O	------	0.15
LOI	------	28
Specific Gravity	3.24	2.46
Crystalline phases present		
Major	Sillimanite	Gibbsite
Minor	Quartz	Anatase

Main detrimental impurities present in bauxite are CaO, Fe_2O_3 and TiO_2 totalling about 12.59% on loss free basis. Specific gravity of bauxite is 2.46 little bit higher than that reported by Grimshaw (2.3-2.4) may be due to the presence of high density anatase. [26] Gibbsite is the main crystalline phase along with anatase minor phase. Linear shrinkage (%) as function of bauxite content (wt.%) is shown in **Fig 4**. Maximum shrinkage is observed at 1600°C with highest bauxite containing batch (SB5). Generation of large volume of liquid phase from impurity present with higher amount of bauxite helps in particle rearrangement and effective packing
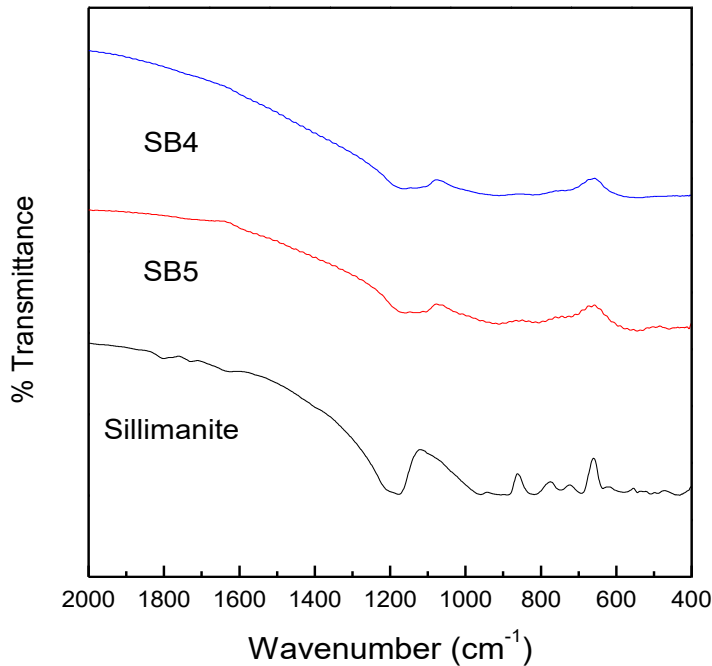
Fig 3: FTIR spectra of raw sillimanite and sintered batch fired at 1550°C/2hr

of particles leading to highest shrinkage (14%). (**Fig 5**) shows the relationship between BD and wt. % of bauxite. Higher the bauxite higher is the BD at all three-sintering temperature. But the change in BD from 40% to 50% bauxite content is steep with respect to the other bauxite content batch. This is may be due to the corundum phase present in the SB5 batch which was detected in powder XRD. Highest BD of 2.82 gm/cc was achieved with 50% bauxite batch (SB5). AP versus bauxite content also reflects (**Fig 6**) the above observation. Larger volume of low melting low viscous glassy phase formed due to presence of higher impurity in bauxite (12.59%) at 1600°C accelerates the pore removal of SB5 batch.
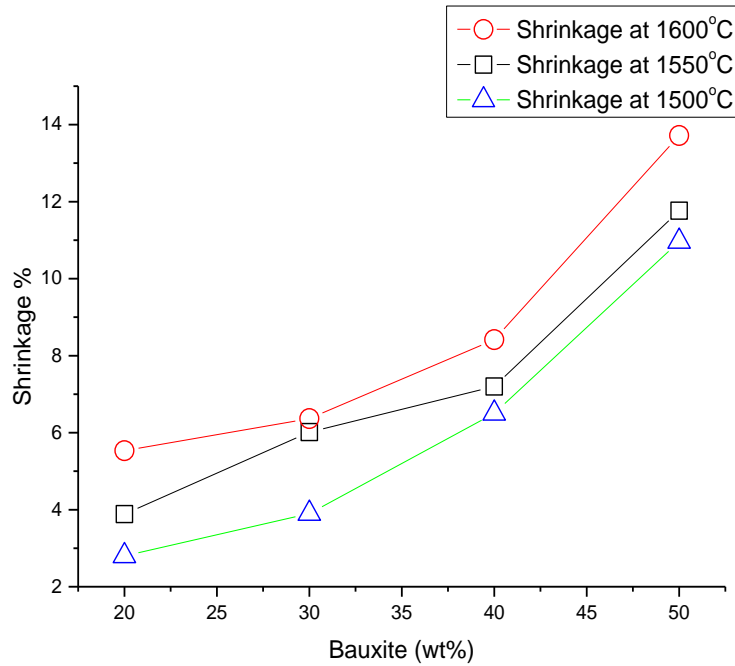
Fig 4: Effect of linear shrinkage (%) on the bauxite content at different sintering temperature
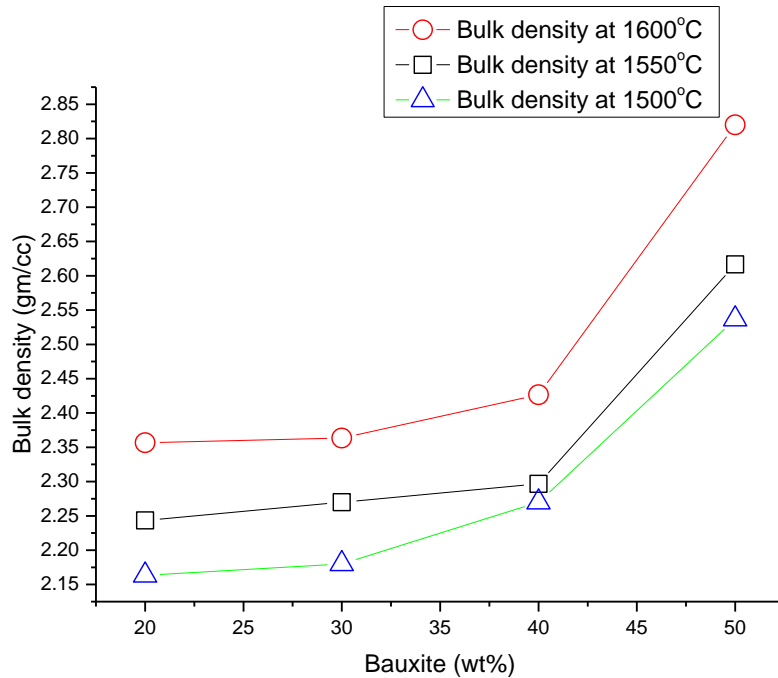
Fig 5: Variation of Bulk Density (BD) with the bauxite content at different sintering temperature
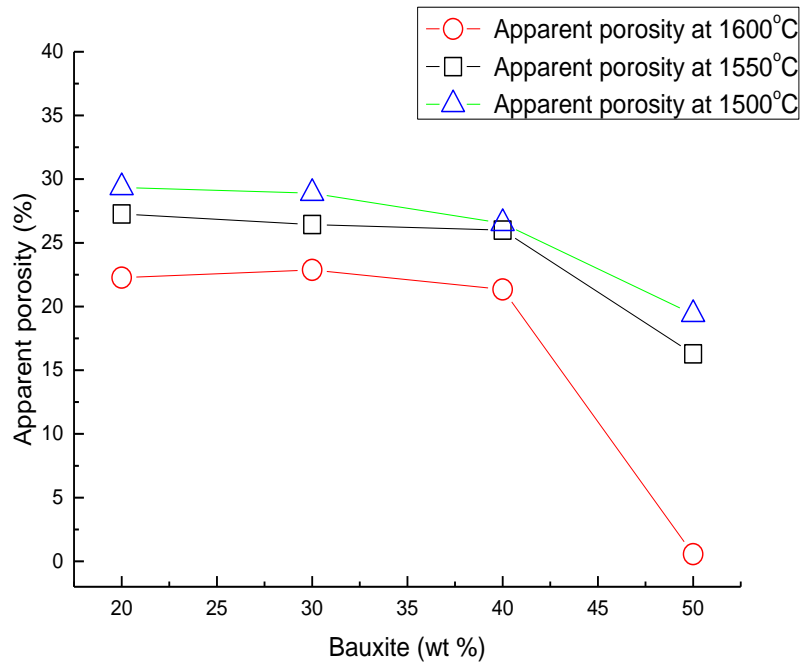
Fig 6: Variation of Apparent Porosity (AP) as function of bauxite content at different sintering temperature

Fig 7 is the powder XRD of SB4 and SB5 samples sintered at $1600^{o}C$/2hrs. SB4 shows mullite as the only main crystalline phase but SB5 containing 50wt% bauxite shows mullite as crystalline phase with few peaks of corundum
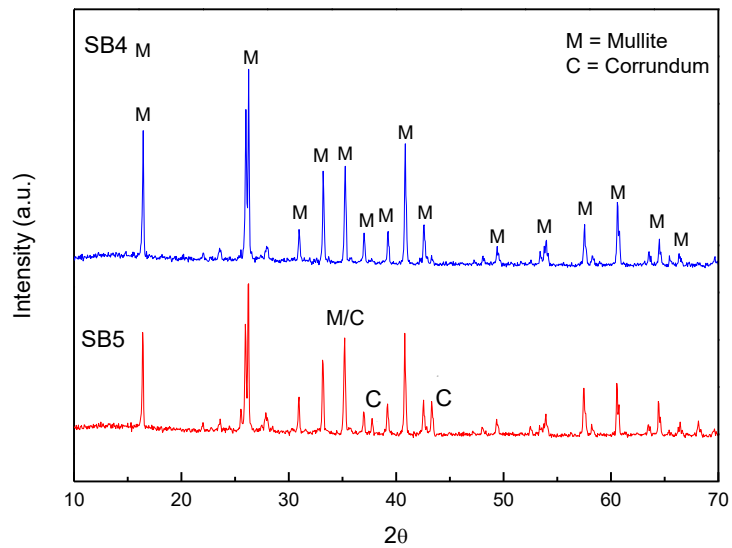
Fig7: Powder XRD pattern of samples sintered at $1550^{o}C$/2hrs

Fig 8 is the secondary electron image of chemically etched fracture surface of SB4 batch sintered at 1600°C/2hr. Elongated columnar shaped grains are mullite. Elongated mullite grains are interlocked. The energy dispersive x-ray analysis shows the presence of titanium, iron, calcium, magnesium, sodium in mullite grains suggesting mullite forms solid solution with these oxides. Glassy phase is also observed with dark colour.
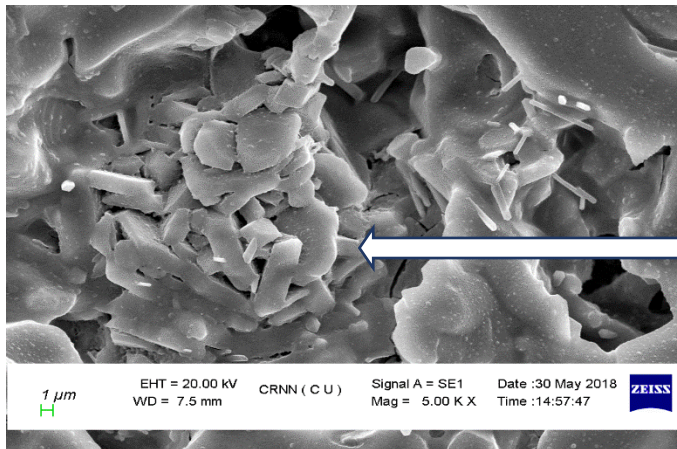
Element	Weight%	Atomic%
O K	37.93	53.36
Na K	1.34	1.31
Mg K	0.51	0.47
Al K	27.78	23.17
Si K	18.66	14.95
Ca K	7.00	3.93
Ti K	1.25	0.59
Fe K	5.53	2.23
Totals	100.00	

Fig 8: Secondary electron image and EDX of SB4 sample sintered at 1600°C/2hrs.

Fig 9 is the secondary electron image of SB5 batch sintered at 1600°C/2hr. Columnar shaped grains are mullite. Equiaxed grains are corundum. EDX analysis shows the amount of titanium, iron, calcium, magnesium, sodium is much high in mullite grain with respect to that in corundum grains.
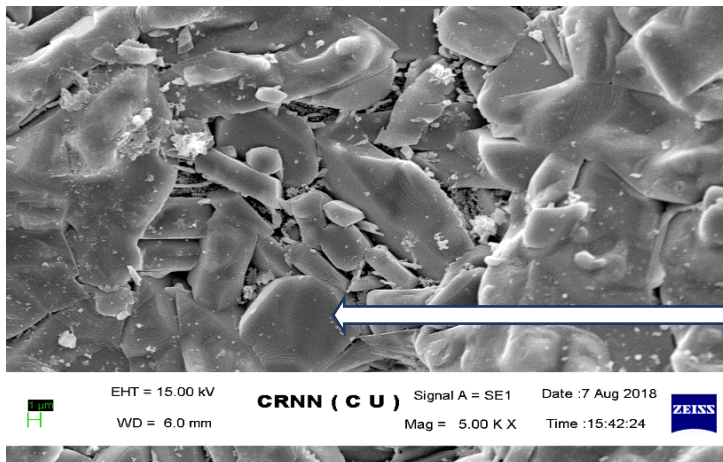
Element	Weight%	Atomic%
O K	46.83	60.32
Na K	0.04	0.04
Mg K	0.35	0.30
Al K	49.89	38.11
Si K	0.43	0.31
Ca K	0.07	0.04
Ti K	0.04	0.02
Fe K	2.34	0.86
Totals	100.00	

Fig 9: Secondary electron image and EDX of SB5 sample sintered at 1600°C/2hrs

Stage -II

From the stage one, we got best properties from alumina rich batch (SB5), that's why we choose SB5 batch and stoichiometric batch (SB4) for next stage.

The chemical analysis of the sintered sample is shown in **Table 4**. The chemical analysis confirms the presence of excess alumina after formation of stoichiometric mullite.

Table 4: Chemical composition of sintered aggregates fired at 1650°C

Parameter (%)	SB4-Z0	SB5-Z0
LOI	0	0
Al_2O_3	67.24	70.05
Fe_2O_3	2.11	2.64
TiO_2	1.37	1.83
CaO	1.51	1.51
SiO2	27.77	23.97

Densification results can be confirmed by measuring linear shrinkage of the compacts. Batches without any ZrO_2 shows lower shrinkage (**fig10-a,b)** with respect to the zirconia containing batches. On increasing firing temperature diametral shrinkage increases. Maximum shrinkage was observed with 50% bauxite containing batch with 5% ZrO_2 content. The value is 15.41% at 1650°C/2hrs.
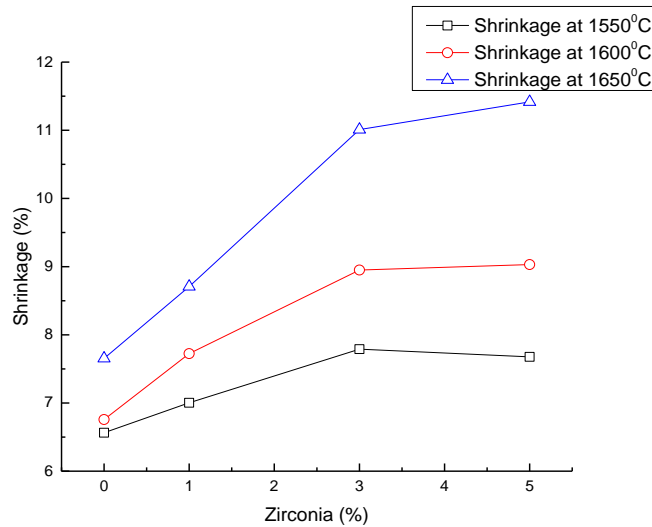
Fig 10(a): Effect of linear shrinkage (%) on the zirconia content and different sintering temperature on 40% bauxite content batch.
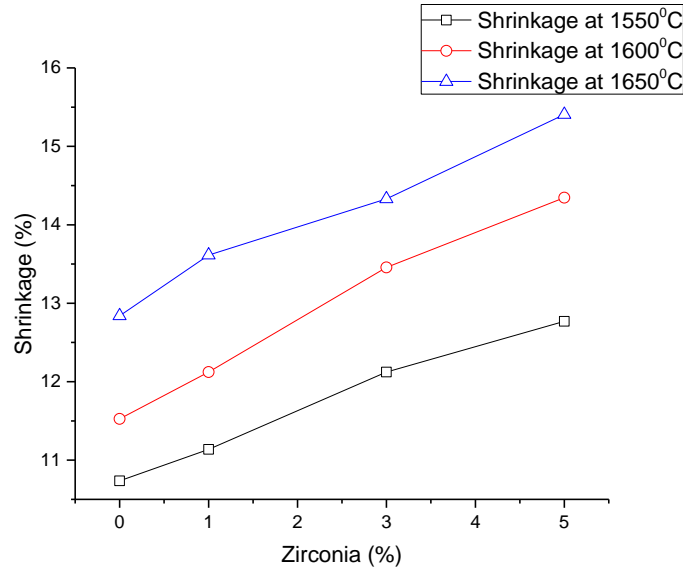
Fig 10(b): Effect of linear shrinkage (%) on the zirconia content and different sintering temperature on 50% bauxite content batch.

The shrinkage value also is also corroborated the value of apparent porosity (**fig11-a,b**). Minimum AP was observed in 50% bauxite batch with 5% ZrO_2 content batch. High percentage zirconia batch may have some pinning effect at the grain bouderies of mullite and corundum resulting in uniform grain size.
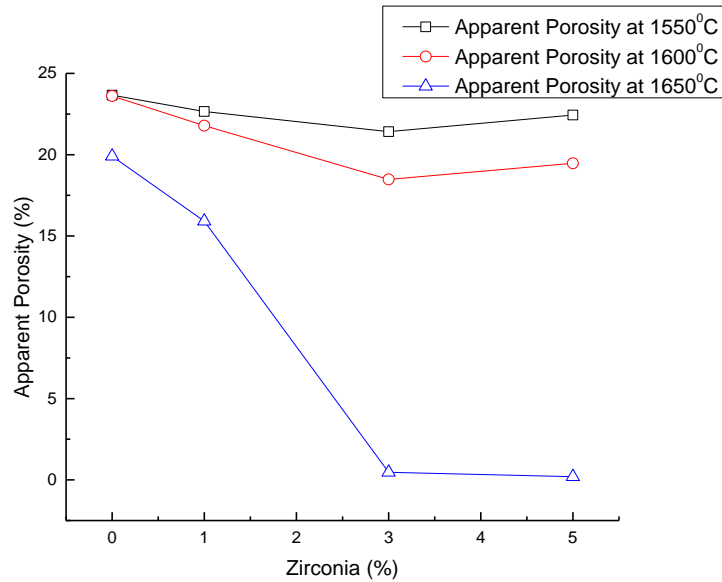

Fig 11(a): Variation of Apparent Porosity (AP) as function of zirconia content at different sintering temperature on 40% bauxite batch
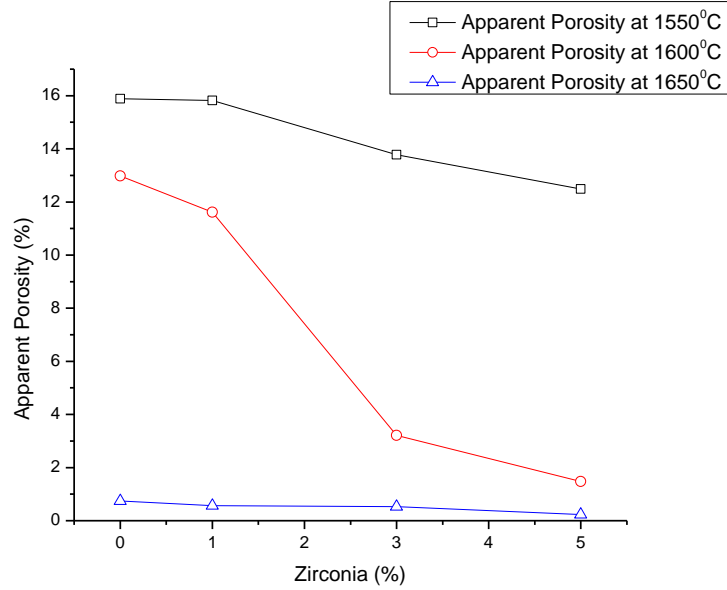
Fig 11(b): Variation of Apparent Porosity (AP) as function of zirconia content at different sintering temperature on 50% bauxite batch

The bulk density (BD) (**fig12-a,b**) of zirconia containing batches are high due to the high density of m-ZrO_2 (5.85 gm/cc) with respect to mullite (3.16 gm/cc) and corundum (3.99 gm/cc). BD of 40% bauxite containing 5 wt.% ZrO_2 is low (2.83 gm/cc) with respect to that of 50% Bauxite containing corundum along with mullite phase.
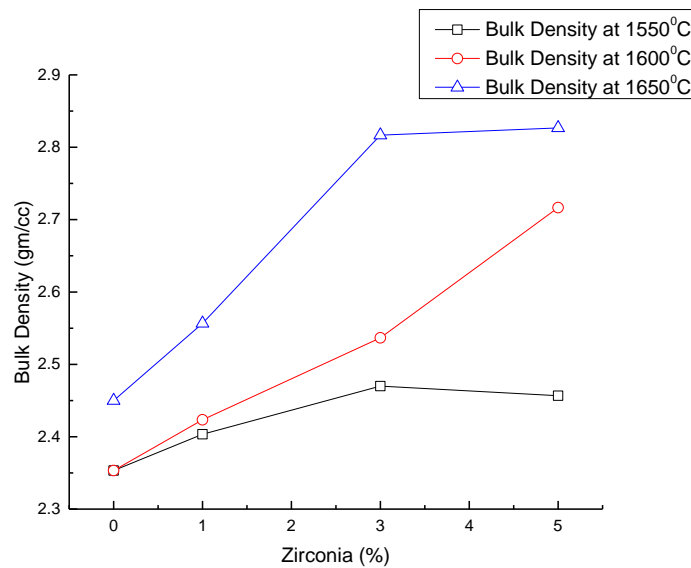
Fig 12(a): Variation of Bulk Density (BD) with the zirconia content at different sintering temperature in 40% batch
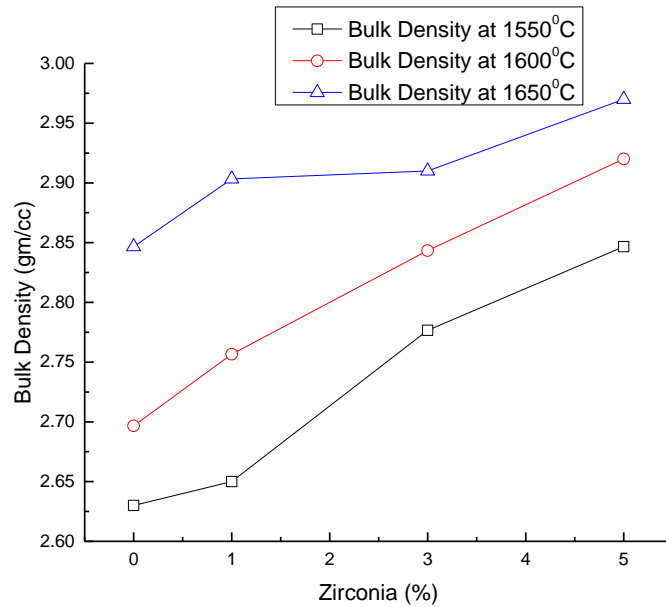
Fig 12(b): Variation of Bulk Density (BD) with the zirconia content at different sintering temperature in 50% batch

The powder x-ray diffraction of SB4-Z5 & SB5-Z5 is displayed in **fig-13.** Zirconia added to both the batches are present as m-Zirconia (01-083-0944). SB5-Z5 batch contain corundum (00-005-0712) along with and m-zirconia. And the major phases are mullite (01-074-2419).
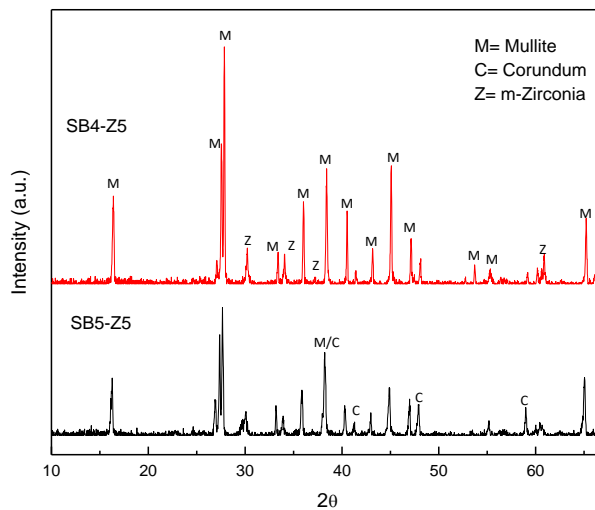

Fig 13: Powder XRD pattern of samples sinteredat 1650ºC/2hrs

FTIR of SB4-Z5 and SB5-Z5 shows (**fig-14**) the presence of double transmittance peaks at 1164 and 1135 cm^{-1} (Al-O & Si-O bond stretching vibration modes) assigned to mullite shows the

formation of this phase from sillimanite [1]. Bonds at 1185 and 950 cm^{-1} (Al-O & Si-O bond stretching vibration modes) are absent confirms the complete decomposition of sillimanite to mullite.
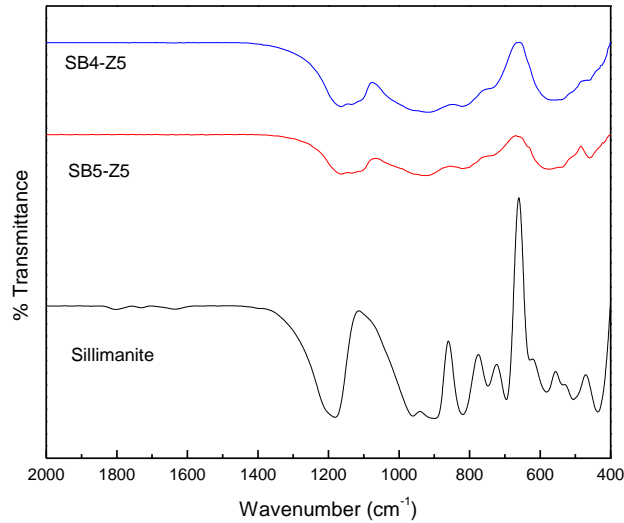

Fig 14: FTIR spectra of raw sillimanite and sintered batch fired at 1650ºC/2hr

Fig-15 is the secondary electron image of chemically etched fractured surface of SB4 batch sintered at 1650℃. Elongated , rounded cornered columnar shaped grains are mullite. Glassy phases are present in the pockets. Black phases may be pores.
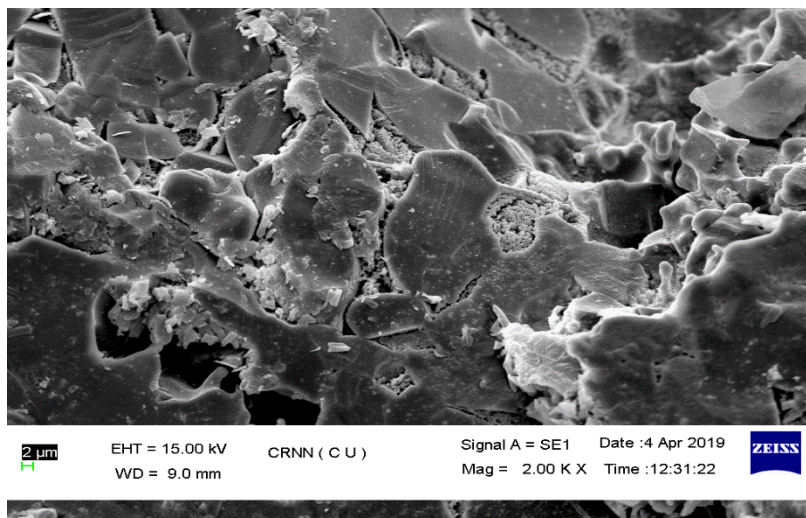
Fig 15: Secondary electron image of SB4-Z0 sample sintered at 1650ºC/2hrs.

Fig-16 is the secondary electron image of chemically etched fractured surface of SB4 with 3 wt% zirconia (SB4-Z3). Mullite grains are angular, equiaxed and small with respect to the previous one.The structure is also compact than the previous one. Glassy phases (granular) arealso observed in the inter-granular space. Grain to grain direct bonding is also notice here. The presence of zirconia changes the morphoslogical of the crystalline phases (changing rounded shaped grain to angular shaped one).
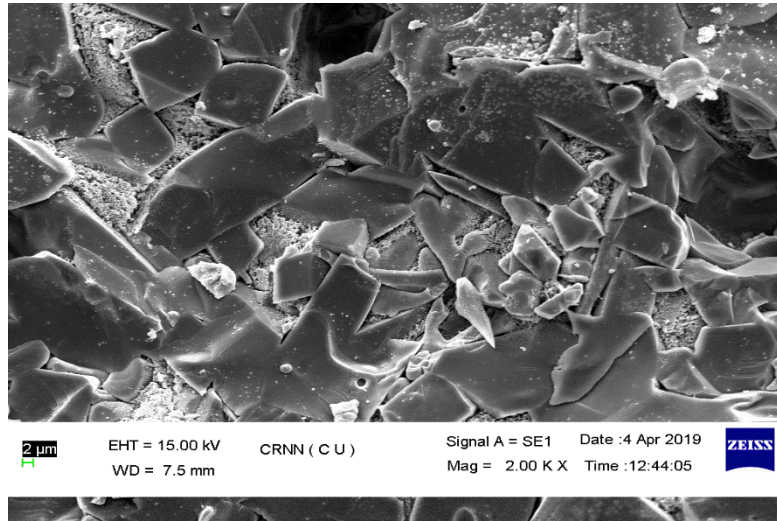

Fig 16: Secondary electron image of SB4-Z3 sample sintered at 1650°C/2hrs.

Fig-17 is the back scattered electron image (BSE) of SB4 batch with 3wt% zirconia. Bright white phases are zirconia wheares angular slate coloured grain are mullite crystals. Direct bonded mullite grains are present. Granular glassy phase is noticed in between the mullite grains.
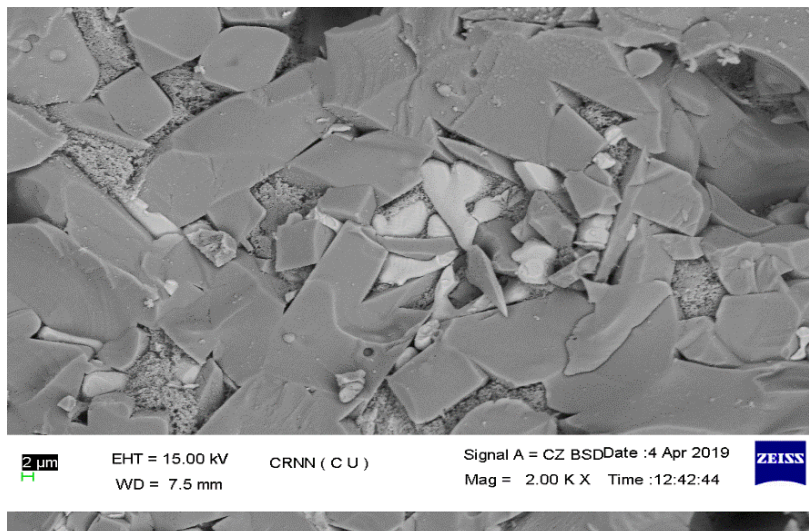

Fig 17: Back Secondary electron image of SB4-Z3 sample sintered at 1650°C/2hrs.

Fig-18 is the secondary image of 50% bauxite containing sillimanite batch sintered at 1650°C/ 2hr. Here the amount of glassy phase is higher with respect to the 40% bauxite batch. The microstructure is compact with low porosity. The mullite grains are rounded cornered elongated.
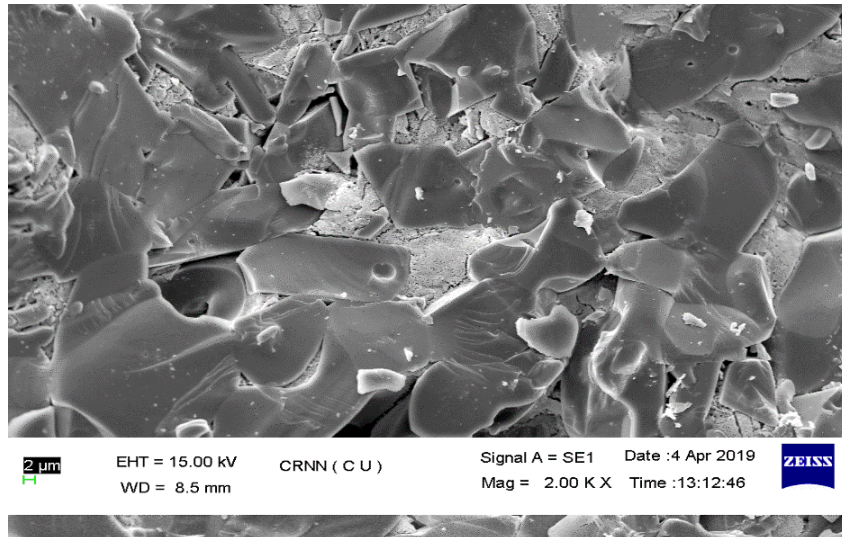

Fig 18: Secondary electron image of SB5-Z0 sample sintered at 1650°C/2hrs.

With the addition of 3 wt% of zirconia to the 50wt% bauxite containing batch (**fig-19**), the grain size are smaller one with respect to the previous one. Here aspect ratio is high and equiaxed grain may be corundum. Pores are not observed here and the structure is compact.
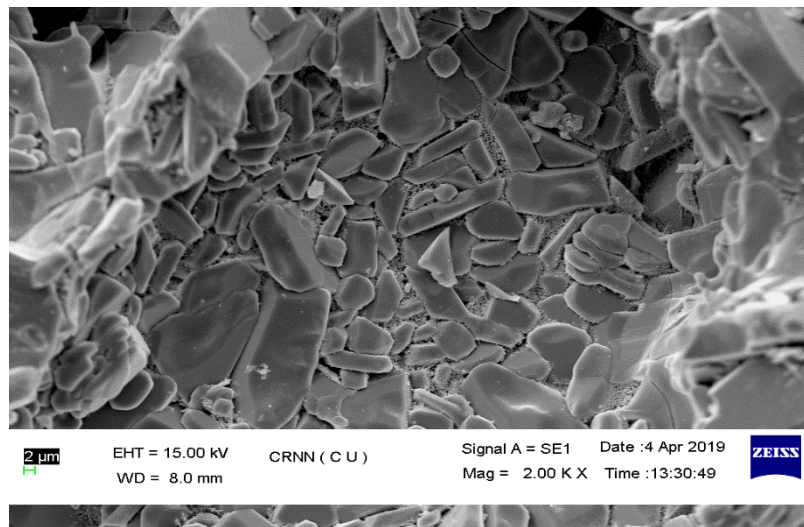

Fig 19: Secondary electron image of SB5-Z3 sample sintered at 1650°C/2hrs.

Furthur addition of ZrO2 (batch SB5-Z5) shows much more elongated mullite with high aspect ratio with sharp corner (**fig-20**). Here the mullite grains are interlocked. Glassy phase (granular) are present in between the crystalline phases. Though it has more glassy phase respect to 40% batch but for this interlocked structure, it has higher CCS value.
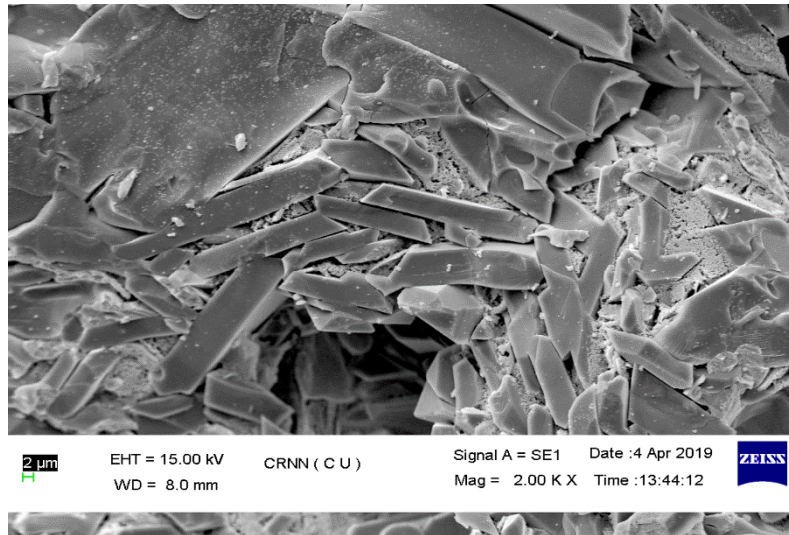

Fig 20: Secondary electron image of SB5-Z5 sample sintered at 1650ºC/2hrs.
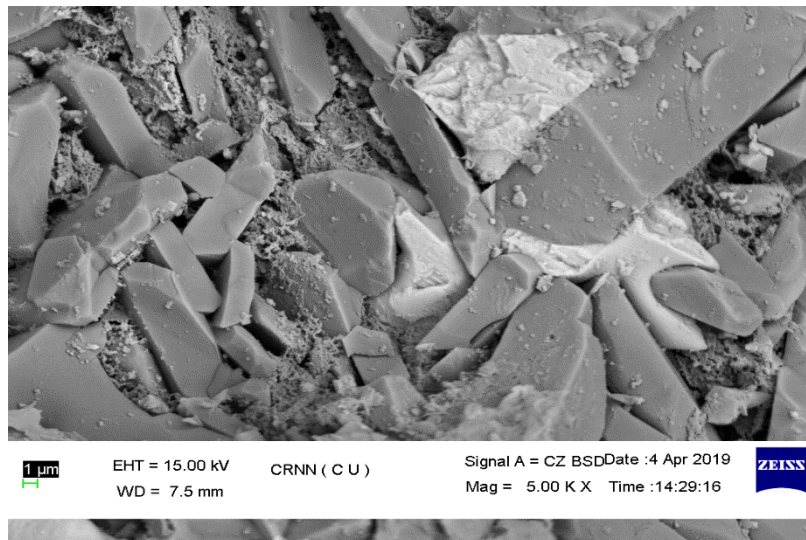

Fig 21: Back Secondary electron image of SB5-Z5 sample sintered at 1650ºC/2hrs

Back scattered electron image (**fig-22**) at low magnification confirmed the uniform distribution of zircon within the matrix.
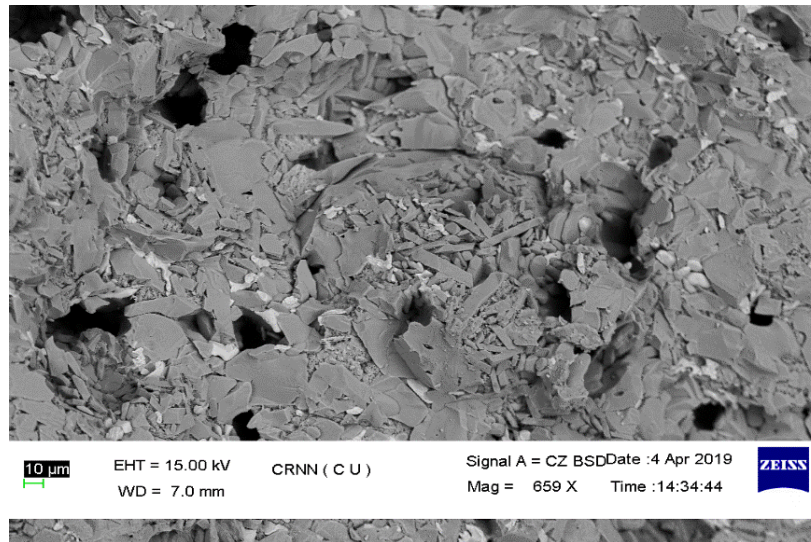
Fig 22: Back Secondary electron image of SB5-Z5 sample sintered at 1600ºC/2hrs

Fig-23 shows the bar chart of slag corrosion resistance of the samples. The figure showed the highest slag resistance in 50% bauxite batch with 5% zirconia. And the 40% bauxite batch without zirconia showed the lowest resistance.   This may be due to the presence of higher amount of porosity in 40% bauxite batch. But zirconia added batches in both 40% and 50% batches showed better slag resistance. The high resistance may be due to the presence of zirconia at the grain boundary.
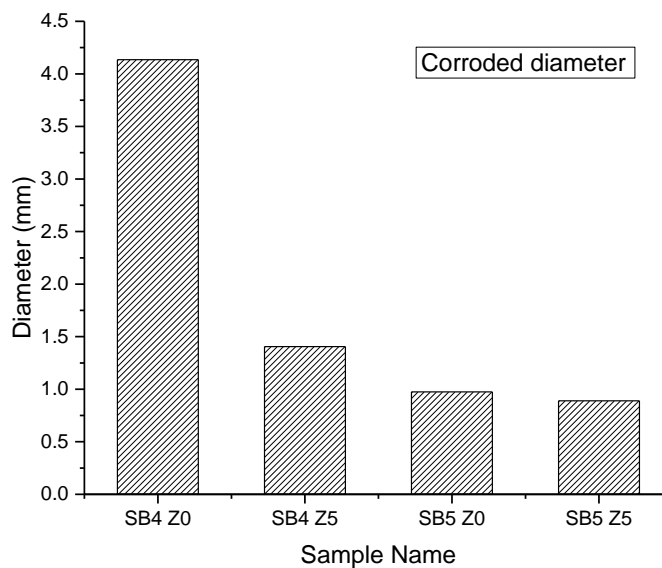

Fig 23: Slag corrosion resistance of sintered samples at 1450ºC/2hrs

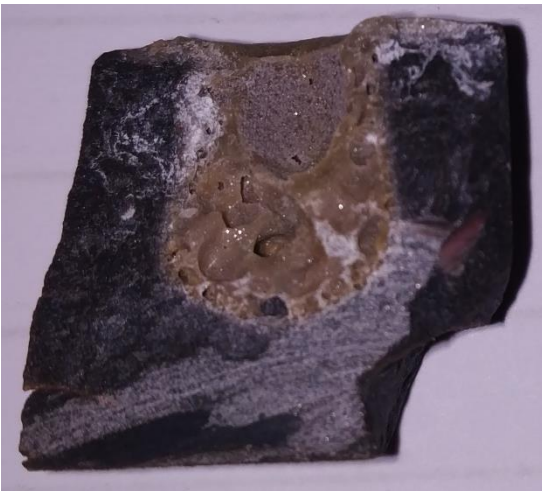<center>(a)</center>

<center>(b)</center>

Fig 24: Cut surface photograph of 40% bauxite containing batch with 0% zirconia (a) and 5% Zirconia (b) after slag corrosion test

<center>(a)</center>

<center>(b)</center>

Fig 25: Cut surface photograph of 50% bauxite containing batch with 0% zirconia (a) and 5% Zirconia (b) after slag corrosion test

CHAPTER 6

SUMMARY & CONCLUSION

6. Summary & Conclusion

Mullite ceramics can be prepared from beach sand sillimanite fine after addition of natural bauxite as alumina source. Higher amount bauxite facilitates the higher sintering rate by providing high amount of liquid phase forming oxide present in bauxite.

Zirconia addition improved the densification as well as the bulk density and it also reduced the apparent porosity. The batch with 5% zirconia and 50% bauxite showed the lowest porosity, highest shrinkage and highest bulk density when sintered at 1650°C. With the higher amount of zirconia bulk density and shrinkage also incresed. But it takes higher sintering temperature to densification.

FTIR of samples shown the presence of double transmittance peaks at 1164 and 1135 cm^{-1} (Al-O & Si-O bond stretching vibration modes) assigned to mullite shows the formation of this phase from sillimanite. Bonds at 1185 and 950 cm^{-1} (Al-O & Si-O bond stretching vibration modes) are absent confirms the complete decomposition of sillimanite to mullite.

High percentage of bauxite addition developed corundum along with mullite crystalline phase. XRD peak showed the presence of mullite ($3Al_2O_3.2SiO_2$) phase, corundum (α-Al_2O_3) phase in 50% bauxite batch and in zirconia added batch, monoclinic zirconia (m-ZrO_2) phase.

Elongated columnar shaped mullite grains were observed in SEM of chemically etched fracture surface. Back scattered electron image (BSE) shows the bright white phases are zirconia wheares angular slate coloured grain are mullite crystals. The presence of zirconia changes the morphology of the crystalline phases (changing rounded shaped grain to angular shaped one). Glassy phases (granular) are also observed in the inter-granular space. Furthur addition of ZrO_2 shows much more elongated mullite with high aspect ratio with sharp corner. Low magnification image confirmed the uniform distribution of zirconia within the matrix.

The EDX analysis shows that the detrimental impurities present in bauxite forms solid solution with mullite. Small amounts of Ti, Fe, Ca, Mg and Na are also detected in corundum grain in higher bauxite content batch (50%).

Zirconia addition showed higher amount of slag corrosion resistance than the non-zirconia batches. PCE shows that the samples can withstand up to 1800°C.

CHAPTER 7

REFERENCE

7.Reference:

1. A. Tomba, M.A. Camerucci, G. Urretavizcaya, A.L. Cavalieri, M.A. Sainz, A. Caballero, **"Elongated mullite crystals obtained from high temperature transformation of sillimanite"**,Ceramics International 25(1999) 245-252.

2. Ibram Ganesh, Govindan Sundararajan, JoseM. F. Ferreira, **"Formation and Densification Behavior ofMullite Aggregates from Beach Sand Sillimanite"**, Journal of American ceramic society 91 [8] 2464–2468 (2008).

3. H. S. Tripathi, B. Mukherjee, S K Das, A Ghosh and G Banerjee, **"Effect of sillimanite beach sand composition on mullitization and properties of Al_2O_3–SiO_2 system",** Bull. Mater. Sci., Vol. 26, No. 2, February 2003, pp. 217–220.

4. H. S. Tripathi, A. Ghosh, M. K. Halder, B. Mukherjee and H. S. Maiti **"Microstructure and properties of sintered mullite developed from Indian bauxite",** Bull. Mater. Sci., Vol. 35, No. 4, August 2012, pp. 639–643.

5. P. Kumar, M. Nath, A. Ghosh, H. S. Tripathi, **"Thermo-mechanical properties of mullite–zirconia composites derived from reaction sintering of zircon and sillimanite beach sand: Effect of CaO",**Trans. Nonferrous Met. Soc. China 26(2016) 2397−2403.

6. S. Rahman, U. Feustel, S. Freimann**, "Structure description of the thermic phase transformation sillimanite–mullite"** Journal of the European Ceramic Society 21 (2001) 2471–2478.

7. H.S. Tripathi, S.K. Das, B. Mukherjee, A. Ghosh, G. Banerjee, **"Synthesis and thermo-mechanical properties of mullite–alumina composite derived from sillimanite beach sand: effect of ZrO_2",** Ceramics International 27 (2001) 833–837.

8. Sasmita Prusty, D.K. Mishra, B.K. Mohapatra, S.K. Singh, **"Effect of MgO in the microstructure formation of zirconia mullite composites from sillimanite and zircon"**, Ceramics International 38 (2012) 2363–2368.

9. Manas K. Haldar, T.K. Pal, G. Banerjee, **"Preparation and properties of Y_2O_3 containing zirconia–mullite composites derived from sillimanite beach sand"**, Ceramics International 28 (2002) 311–318.

10. Michael D. Sacks, Joseph A. Pask, **"Sintering of Mullite-Containing Materials: I, Effect of Composition"**, Journal of the American Ceramic Society, Volume 66, Number 2 February 1982.

11. F. Cambier, C. Leblud, M. R. Anseau, A. Leriche,**"High temperature mechanical properties of reaction-sintered mullite/zirconia and mullite/alumina/zirconia composites"**, Journal of Materials Science 20 (1985) 2533—2540.

12. Mingwei Yan, Yong Li, Yang Sun, Ling Li, Shanghao Tong, JialinSun,**"Controllable preparation and synthetic mechanism of mullite from the bauxite with Fe-rich oxide content"**,Material Chemistry and Physics 202(2017)245-250.

13. S. Prusty, D. K. Mishra, B. K. Mohapatra and S. K. Singh, **"Correlation between properties of zirconia mullite and Y_2O_3 stabilized zirconia mullite derived by various processing techniques"**, Advances in Applied Ceramics, Vol. 110 (2011) 360-366.

14. Manas Kamal Haldar**, "Effect of magnesia additions on the properties of zirconia–mullite composites derived from sillimanite beach sand"**, Ceramics International 29 (2003) 573–581.

15. Philippe Descamps, Shuji Sakaguchi, Marc Poorternan, and Francis Cambier, **"High-Temperature Characterization of Reaction-Sintered Mullite-Zirconia Composites"** journal of American ceramic society 74 [10] 2476-81 (1991).

16. Manas K. Haldar, G. Banerjee, **"Properties of zirconia–mullite composites prepared from beach sand sillimanite"**,Materials letter 57 (2003) 3513-3520.

17. Atul V. Maldhure, Himansu S. Tripathi, Arup Ghosh, **"Mechanical Properties of Mullite–Corundum Composites Prepared from Bauxite"**,Int. J. Appl. CeramTechnology, 12 [4] 860–866 (2015).

18. Qiang Ren, Huanhuan Li, Xiulan Wu, Zhe zhe Huo, Ou Hai, Fei Lin, **"Effect of the calcining temperatures of low-grade bauxite on the mechanical property of mullite ceramics"**, Int J Appl Ceram Technol. 2017,1–9.

19. Yingchao Dong, Xuyong Feng, Xuefei Feng, Yanwei Ding, Xingqin Liu, Guangyao Meng, **"Preparation of low-cost mullite ceramics from natural bauxite and industrial waste fly ash"**, Journal of Alloys and Compounds, 460 (2008) 599–606.

20. Toshiyuki Koyama, Shigeo Hayashi, AtsuoYasumori, Kiyoshi Okada, **"Preparation and Characterization of Mullite-Zirconia Composites from Various Starting Materials"**, Journal of the European Ceramic Society 14 (1994) 295-302.

21. H. S. Tripathi, S. K. Das, B. Mukherjee, A. Ghosh, **"Sintered Mullite from Aluminous Ore for Refractory Application"** American Ceramic Society Bulletin, Vol. 86, No. 5 (9301-9304).

22. H. Schneider, J. Schreuer, B. Hildmann, **"Structure and properties of mullite—A review"**, Journal of the European Ceramic Society 28 (2008) 329–344.

23. M.M.S. Wahsh, R.M. Khattab, M. Awaad **"Thermo-mechanical properties of mullite/zirconia reinforced alumina ceramic composites"**, Materials and Design 41 (2012) 31–36.

24. Cemail Aksel, **"The role of fine alumina and mullite particles on the thermo mechanical behavior of alumina–mullite refractory materials"**, Materials Letters 57 (2002) 708 – 714.

25. H. Schneider**, "Solubility of TiO_2, Fe_2O_3 and MgO in Mullite"**, Ceramics International 13 (1987) 77-82.

26. **The chem. And Physics of clay and allied materials**by R.W. Grimshaw (London, Ernest Benn Ltd) 4th ed p 329.